

Characterization of a superconducting nanowire single photon detector

Max Reicherd

Bachelorarbeit in Physik
angefertigt im Institut für Angewandte Physik

vorgelegt der
Mathematisch-Naturwissenschaftlichen Fakultät
der
Rheinischen Friedrich-Wilhelms-Universität
Bonn

Juli 2024

I hereby declare that this thesis was formulated by myself and that no sources or tools other than those cited were used.

Bonn,
Date
Signature

1. Reviewer: Prof. Dr. Sebastian Hofferberth
2. Reviewer: Prof. Dr. Daqing Wang

Acknowledgements

I would like to thank all members of the Nonlinear Quantum Optics group of the University of Bonn. It was a pleasure to be part in this group and I learned a lot of new interesting physics. Also, I want to thank the members from the HQO experiment, especially Julia Gamper, Leon Sadowski and Cedric Wind for the nice atmosphere and support in my work. Especially, at the final phase of my thesis. I would also like to thank Prof. Sebastian Hofferberth for the opportunity to write my thesis and continue working in his group. At the end I would like to thank my family and partner for the support and the patience during my studies.

Contents

1	Introduction	1
2	Working principle of a SNSPD	2
3	Faint laser source for detector characterization	6
3.1	Characteristics of faint laser sources	6
3.2	Experimental setup	7
3.3	Neutral density filter calibration	8
4	Characterization of a SNSPD by Single Quantum	10
4.1	Dark count rate	10
4.2	Recovery time	12
4.3	Efficiency	17
4.4	Summary of the results	25
5	Summary and Outlook	26
A	Appendix	28
A.1	Set up and elements	28
A.2	Neutral density filter calibration - Error calculation	30
A.3	Angle dependent count rate measurement data and results	34
A.4	Count rate dependent efficiency η_{sde}	34
A.5	Bias sweeping for different count rates	35
A.6	Recovery time measurements	36
A.7	Recordings of analog pulses	37
Bibliography		39

CHAPTER 1

Introduction

Single photon detectors enable the study of optical interaction on the single photon level which makes them a powerful tool for many quantum experiments [**charaev-2023**].

CHAPTER 2

Working principle of a SNSPD

This chapter will introduce the working principle of superconducting nanowire single photon detectors (SNSPD). This chapter is structured in three parts. The first part describes the essential detector elements and their functions. The second part explains the detection process and provides its principles in terms of their phenomenological aspects. For further details regarding the physics and mathematics behind superconducting nanowires, the reader is directed to the work of Gol'tsman et al. [7] and Hadfield et al. [8]. The third part will explain the reason why the detected photons need to be aligned to the slow axis of the optical fibre.

In general a SNSPD consists of four parts, as shown in figure 2.1. The most important part is detection area and consists of a superconducting nanowire ($\approx 100\text{nm}$ wide) on a sapphire base. In general, superconductors have the property of abruptly losing all internal resistance once the temperature T_{krit} falls *below* a critical temperature. If the critical temperature is *exceeded* (e.g. due to the environment or excessive current), the resistance suddenly increases again. Theoretically, this behaviour is described using Cooper pairs in the BCS theory [9]. A more detailed description of superconductors is omitted in this chapter. To collect the entire output of the optical fibre, a pattern of a thin superconducting film (such as niobium nitride) is shaped into a meandering nanowire by nanofabrication [10]. Another element is the sapphire layer, which is used to dissipate the heat when the wire heats up. Further, a gold contact supplies a bias current through the superconducting nanowire, and an optical fibre is coupled to the detection area. To operate the system, this setup is cooled below the critical temperature of the superconductor to 2-3K and a DC current (Bias current I_B) is applied to the superconducting nanowire.

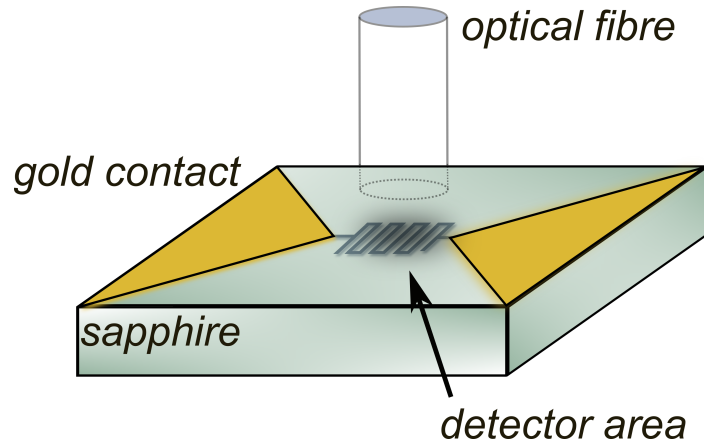


Figure 2.1: Scematic illustration of the fundamental parts of a superconducting nanowire single photon detector based on [11]. Detector area is made of a superconducting nanowire and is contacted with gold from two sides. An optical fibre is coupled to the detector area. The fibre coupling realization of the characterized detector from Single Quantum is shown in figure 2.4.

In this second part, the detection process, shown in figure 2.2 is outlined. Starting point (i) is the detector area in the superconducting state and an applied Bias current which is below the critical current. Then, if photons hit the superconducting nanowire (ii), they break up individual Cooper pairs. This leads to a local reduction of the critical current below the bias current and in turn to a localized area, where the superconductivity is interrupted. This local area forms the so-called "hotspot" (iii). This hotspot forms a resistance area because the critical temperature is exceeded by the energy of the photon. In response, the current flows around this hotspot (iv), whereby the local current density in the side areas next to the hotspot again exceeds the critical current, due to a higher current density. If the critical current is exceeded, the superconductivity also breaks down in these areas. The excess also causes a resistance in the side channels of the nanowire (v). This rapid increase in resistance can ultimately be measured in form of a voltage pulse, which can be seen in figure 2.3. The local non-superconducting area is then cooled down by the cryogenic environment and returns to the superconducting state (iv—i).

In the detection process the photon polarization plays a crucial role. Due to a polarization dependent absorption efficiency, it is important to consider the technical detail of the geometry of the meander. In the used SNSPD, the meander design allows for a higher absorption efficiency if the E-field of the photons is polarized parallel to the wire direction rather than orthogonally polarized [10]. As depicted in figure 2.4 the slow axis of the coupled fibre in the characterized detector is aligned parallel to the nanowire to maximize the absorption efficiency. Other geometries are being investigated and might enable a high absorption efficiency independent of polarization [13].

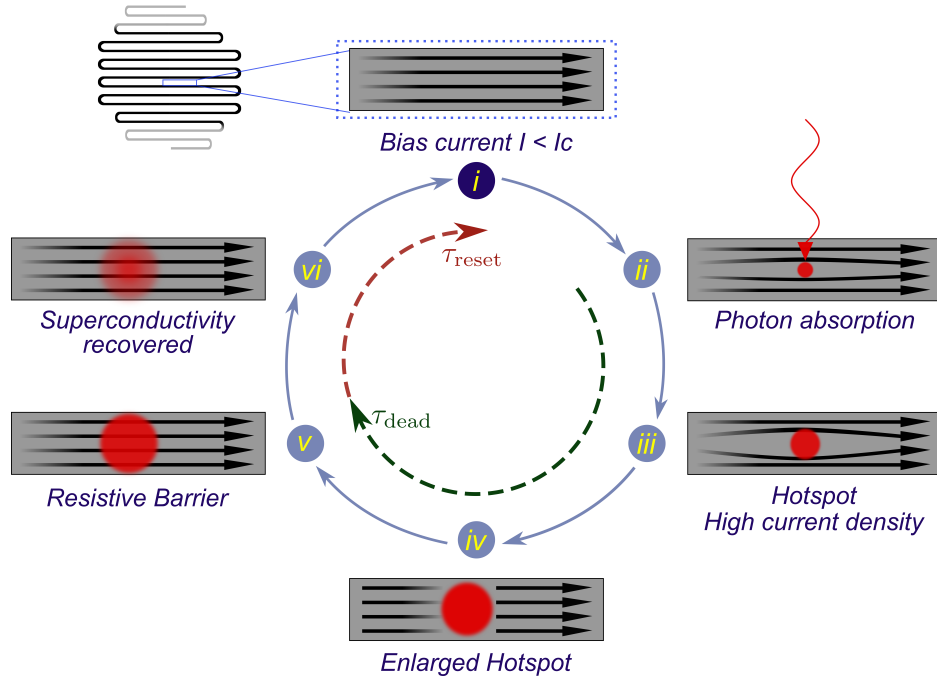


Figure 2.2: Schematic detection process cycle of a superconducting nanowire single photon detector based on [12]. The dotted innercircle shows the parts of the dead time τ_{dead} and the reset time τ_{reset} . The outer circle shows the parts of the detection process. In the upper left side the whole detector area is shown, the grey bars show the current flow in the zoomed superconducting nanowire.

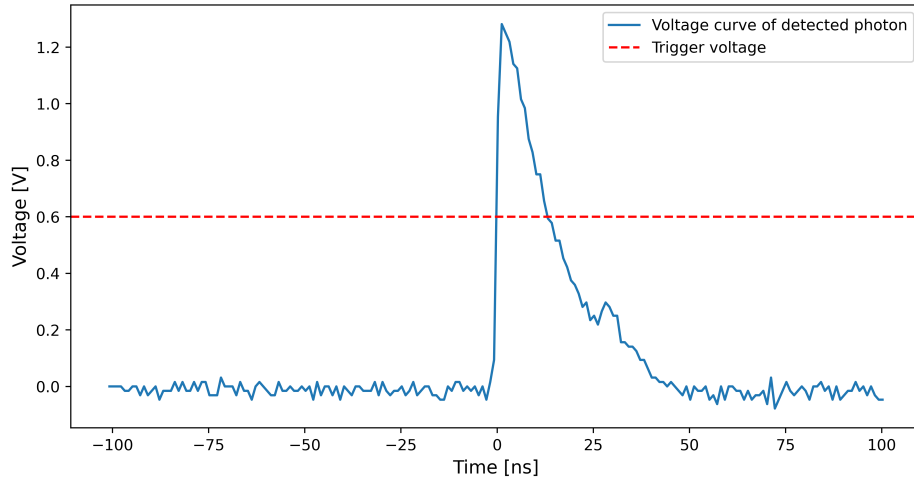


Figure 2.3: Single analog voltage pulse signal, recorded with a Lecrois oscilloscope with a time resolution of 500MHz. Voltage is depicted on the Y-axis and time in ns on the X-axis. A single photon steems from a faint laser source (780nm) attenuated to a photon rate of 1.772KHz.

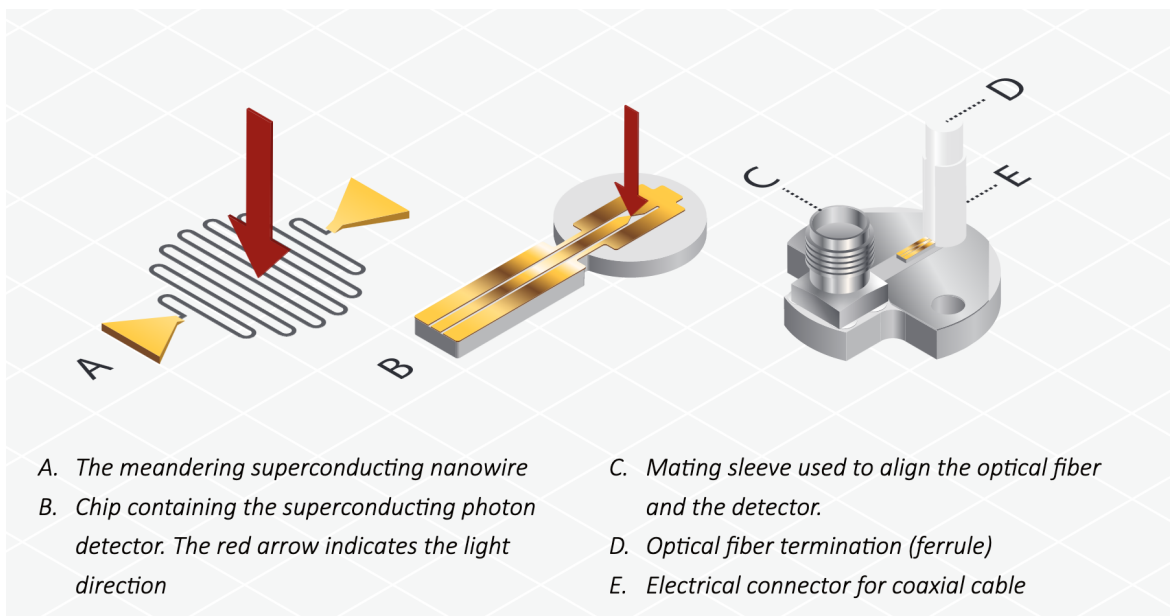


Figure 2.4: Fibre coupling set up to the superconducting nanowire detector area of the characterized detector from the Single Quantum [14]. Fibre coupling is made in-house and is adjusted to maximize efficiency. It cannot be adjusted manually.

CHAPTER 3

Faint laser source for detector characterization

In order to characterize a detector, it is necessary to consider not only the characteristics of the detector itself, but also those of the emitter source. This section will focus on the characteristics of the laser setup, which serves as a coherent light source for the detector characterization. A brief overview of the characteristics of a coherent laser light source and the conditions it gives for detector characterization will be provided. Furthermore, the setup of the faint laser source that has been constructed for characterizing the SNSPD will be introduced. At the end the calibration of the neutral density filters will be discussed.

3.1 Characteristics of faint laser sources

The emitting light from a laser is considered as monochromatic beam with frequency f and constant intensity I . The average rate Φ of a laser is given by:

$$\Phi = \frac{P}{hf} \quad (3.1)$$

where P the laser power. h plancks constant and $f = \frac{c}{\lambda}$ the frequency which depends on the wavelength. c is the speed of light. The average number of registered counts $N(T)$ for a given detection time T by a detector is given by:

$$N(T) = T\Phi\eta = \frac{PT\eta}{hf} \quad (3.2)$$

where η is the efficiency of the detector system which is described in more detail in section 4.3.

Since, we are interested in detecting single photons, the photon rate has to be low, which corresponds to $N(T) \cdot \eta \ll 1$ [15].

Based on this, for an ideal detector with a recovery time of zero the registered counts \mathcal{R} per unit time are:

$$\mathcal{R} = \frac{N(T)}{T} = \eta\Phi = \frac{P\eta}{hf} \quad (3.3)$$

However, for a real detector the true count rate is restricted by the dead time τ_d and the dark count rate of the detector. Therefore, the true count rate \mathcal{R}' is given by:

$$\mathcal{R}' = \left(\frac{\mathcal{R}}{1 - \tau_d \cdot \mathcal{R}} - \frac{DCR}{1 - \tau_d \cdot DCR} \right) \quad (3.4)$$

where τ_d is the dead time of the detector and DCR is the dark count rate of the detector.

Furthermore, the maximal count rate of the detector is restricted by the dead time τ_d . In addition sending too many photons at once to the detector causes latching and prevents counting [10].

3.2 Experimental setup

As mentioned above, we are interested in detecting single photons, corresponding to $N(T) \cdot \eta \ll 1$ [15]. Therefore, the laser power has to be low enough to detect single photons. The minimum laser power of the laser source is higher than the maximum detection count rate of the detector. The reason for this is that the laser source only starts to lase given a minimum input power. Therefore, the laser power can not be regulated down by adjusting the input power of the laser, but has to be attenuated by neutral density filters.

In order to realize the laser attenuation the setup shown in figure 3.1 and section A.1 was build. The starting point is the upper stage (left) and the optical axis runs parallel to the table. Laser light is emitted from a 780nm laser source from the Russian company Vitawave and is coupled into a single mode polarization maintaining fibre. The quarter-wave plate λ_4 and half-wave plate λ_2 were used to set the polarization of the light vertical to the optical axis. The laser beam was coupled at the upper stage, such that it could be used at the lower stage.

Afterwards, on the lower stage the beam passes a half-wave plate λ_2 and polarization beam splitter (pbs) to filter the horizontal polarized E-field out. Further, a Galilean telescope was built with one focal (l_1) and one diffusing lens (l_2) to reduce the beam width. This reduction was done to not exceed the surface of the crystal of the Acousto-optic modulator (AOM). After the AOM, a cover was used to select the first order of the AOM. The first order of the AOM was used for flexible intensity modulation of the laser. Then a flip mount was placed where anti reflection coatet (AR) neutral density (ND) filters could be set in and out of the laser beam. The ND filters have the function to attenuate the laser light.

Before the laser light was again coupled in the optical fibre, another half-wave plate λ_2 and a quarter-wave plate λ_4 were used to control the light polarization coupling in the fibre. As mentioned in section 2 the light was polarized according to the slow axis of the fibre. Afterwards the light is coupled into the fibre, guiding it to the detector.

Regarding the final coupling it was important, to couple the light to an APC/PC (fibre channel / angled physical contact) to FC/PC (fibre channel / physical contact) optical fibre. The coupling from the experiment to a APC/PC optical fibre was done because it yields lower reflection losses. On the other side, the detector had only an FC/PC optical fibre input port, in order to maintain higher

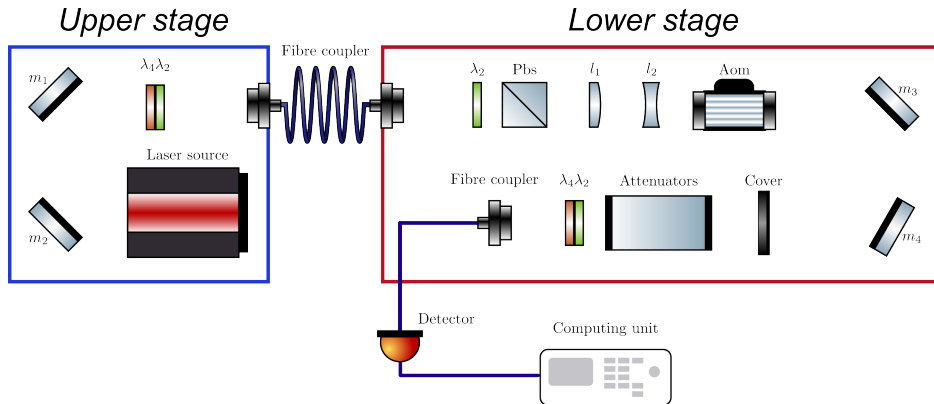


Figure 3.1: Set up for attenuation of a 780nm laser source from the Russian company Vitawave.

efficiency coupling [10].

Besides, this optical setup had to be protected from environmental light. For this, the windows in the room, where the setup was installed were shielded with aluminium foil which has a reflection coefficient of almost 90% at the operating wavelength of 780nm [16]. Moreover, an optical enclosure (black box) was made from black plexiglass and wood (seen in section A.1), where the optical setup was placed in.

It has the function to avoid environmental light coupling into the fibre. Additionally, the optical fibre going from the optical setup to the detector was covered with aluminium foil to avoid absorption of stray light through the cladding.

3.3 Neutral density filter calibration

Based on those theoretical considerations and the experimental setup, one can approach the central goal to determine the amount of photons and with this, determine the efficiency of the detector.

In order to do efficiency measurements, one must send only a few photons (low power) and one must exactly know how many photons are sent. For this the power of the laser light sending to the detector needs to be measured.

However, the desired light is so weak, one cannot measure it with power-meters or any other measurement devices available to us. Therefore, the expected photon rate sent to the detector depends on the ND filters and their optical density (OD) value. Since no time was left to characterize the AOM, the ND filter were the sole factor to adjust the photon rate, given a stable laser power.

The challenge relying on ND filters is that the fabric values of their OD are not precise. Thus, the filters need to be calibrated to get accurate OD values for the ND filters. The OD value of each filter is measured with two methods to account for systematic errors. In the first method (method 1) the ND filters are set in the flip mount as shown in graph 3.1. In the second method (method 2), measurements with and without filters were done directly in front of the powermeter outside the black box to avoid straying light inside the black box. See figure ?? for pictures of how this was realized.

The attenuation of ND filters is quantized by the OD value and is connected to the transmission

value $T_{ND} = 10^{-OD}$ of the outgoing light. Due to the logarithmic definition of the OD value ($OD = \log_{10}(\frac{1}{T_{ND}})$), the OD values of the ND filters are added up when they are stacked on each other.

The measurement of the OD values was done by measuring the power with and without the filter. Moreover, only measurements for one single ND filter were done. The reason is the measurable range of the power metre. The power meter was unable to accurately measure the power of the attenuated laser light through more than one ND filter.

The transmission then corresponds to:

$$T = \frac{P_{ND}}{P} \quad (3.5)$$

where, P_{ND} is the power of the laser light with the applied ND filters. P is the power of the laser light without the ND filters.

The final OD values of each method were combined and the corresponding systematic and statistical errors are considered in order to get accurate OD values for the ND filters. Results of the measurements and error calculations can be found in section [A.2](#). Based on these OD values the photon rate was determined.

CHAPTER 4

Characterization of a SNSPD by Single Quantum

In literature, four central characteristics have emerged to quantify the quality of single photon detectors and make their performances comparable [8, 15]. These characteristics are the system detection efficiency (η_{sde}), the dark count rate (DCR), the recovery time ($\tau_{\text{recovery}} = \tau_{\text{rec}}$) and the timing jitter (Δt). In this chapter, I investigate the detector efficiency (η_{sde}), the dark count rate (DCR) and the recovery time (τ_{rec}). At the end, the results will be summarized and discussed. The timing jitter (Δt) was not analyzed due to missing equipment like a fast pulse laser and time constraints. In general there are more than these introduced quantities, like after-pulsing but these will not be considered in this thesis.

4.1 Dark count rate

The DCR is the rate of false positive events which are not intentionally generated from the source (here the faint laser source). It is measured in counts per second and can be caused by statistical fluctuations in the measurement electronics. A low DCR is important for a high signal-to-noise ratio and means easy interpretable results which are not distorted by noise [17].

In the context of SNSPDs, the DCR is dependent on the bias current applied to the nanowire. This is due to the fact that if the bias current approaches the critical current, less current $\Delta I = I_c - I_B$ is needed to exceed the critical current .

Therefore, thermal electronic fluctuations, close to the critical current will cause a breakdown of the superconducting state and hence more dark counts are detected. It is important to perform DCR measurements first in the characterization process because it determines the bias current limit, where general measurements are not distorted by high DCR.

Measurement and results

In order to evaluate the DCR, it is necessary to perform measurements in two different setups. In the first setup no optical fibre is connected to the detector and the detector port is covered with a protection cap. In such a setup, it can be assumed that no photons from the environment strike the detector. This allows for measurements of the DCR only triggered by thermal electronic fluctuations and depending on the detector's bias current. This configuration represents the most shielded environment from external light sources and serves as reference value for the lowest DCR values. The measurement

was conducted by sweeping the bias current from 0 to $35\mu\text{A}$, at a trigger voltage of 200mV in $0.1\mu\text{A}$ increments with an integration time of 200ms at each step.

In the second setup the detector is connected with an optical fibre to the faint laser source (introduced in section 3.1). The set up stands in free space and the laser source was turned off, so no photons from the source were sent to the detector. The orange curve in 4.1 demonstrates that in the absence of any protection, a significant number of photons from the environment are able to enter the detector through various potential pathways like the fibre cladding or the coupling connection to the laser setup.

To reduce dark counts due to ambient light a black box was constructed (as discussed in section 3) that covers the laser setup. Further, the optical fiber was wrapped in aluminum foil to prevent ambient light coupling to the core through the cladding. Once more, the bias current was swept from 0 to $35\mu\text{A}$ in $0.1\mu\text{A}$ increments with an integration time of the count rates for 200 ms . In figure 4.1 the results for this optimized case are shown by the green curve.

The measurement results for the optimized case show that the DCR of the coupled and protected setup are the same as the DCR with the protection cap on. The peaks in the green curve at $\approx 3\mu\text{A}$ and $\approx 14\mu\text{A}$ are artifacts resulting from some leakages in the protection. Nevertheless, these leakages are not substantial when viewed in the context of the total photon count rate. Particularly, when considering anticipated photon rates from the faint weak laser source in the high kHz and MHz range.

One can conclude from the investigation of the DCR of channel 1 that all further measurements should be done at a bias current below $I_B < \approx 31.2\mu\text{A}$. As mentioned above, the final DCR is depending on the bias current working point. Therefore, five 60s measurements were done for three different bias currents ($24\mu\text{A}$, $28\mu\text{A}$ and $31.2\mu\text{A}$). The averaged results for channel one of the detector yield a DCR of:

$$DCR_{24\mu\text{A}} = (1.40 \pm 1.02)\text{Hz} \quad (4.1)$$

$$DCR_{28\mu\text{A}} = (1.20 \pm 0.98)\text{Hz} \quad (4.2)$$

$$DCR_{31.2\mu\text{A}} = (1.40 \pm 1.36)\text{Hz} \quad (4.3)$$

where the error is the standard deviation of the mean. These results are in agreement to the companies specifications of: $DCR < 5$ [6].

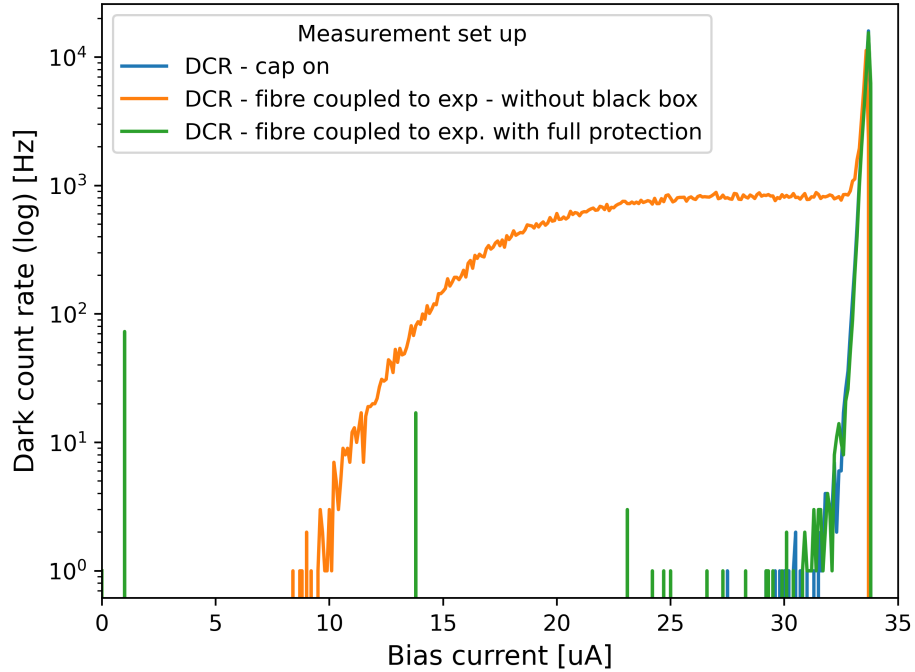


Figure 4.1: Channel 1 DCR measurements for different bias currents at a trigger voltage of 200MHz. The blue curve shows the DCR with a cap on the output port of the detector. The orange curve shows the DCR with an optical fibre connected to the detector and the experiment (in free space). The green curve shows the DCR with an optical fibre connected to the detector and the experiment (in a black box). Additionally, the optical fiber was wrapped in aluminum foil.

4.2 Recovery time

The concept of the recovery time is visually depicted in figure 4.2. When a photon hits the detector and is absorbed, the efficiency (η_{sde}) of the detector drops to zero and *no further photons* can be measured for a certain period of time. This elapsed time is called the dead time ($\tau_{\text{dead}} = \tau_d$). The efficiency then rises again to the original system detection efficiency (η_{sde}). This period is called the reset time ($\tau_{\text{reset}} = \tau_r$). The vertical dashed line forms the starting point where the efficiency rises again to the system detection efficiency (η_{sde}). Finally, the sum of both times forms the recovery time ($\tau_{\text{rec}} = \tau_r + \tau_d$).

The recovery time is important because it determines the temporal resolution of the detector [15]. The temporal resolution describes the minimal time interval where the detector can distinguish between two photons. The lower the recovery time, as higher is the temporal resolution, or maximal count rate of the detector.

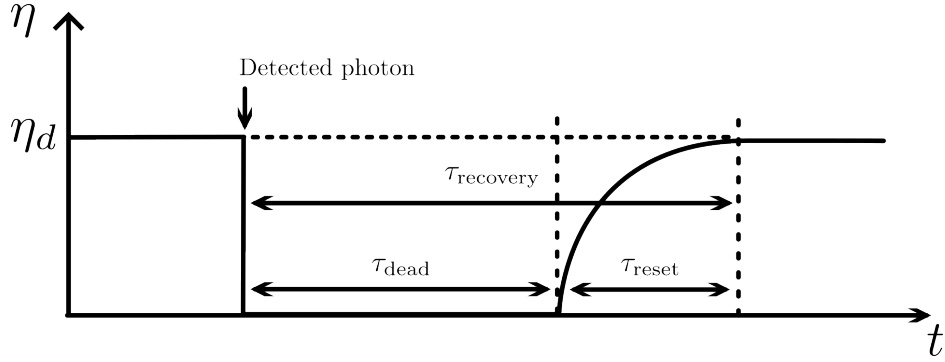


Figure 4.2: Schematic efficiency curve for the detection of a photon[18]. On the Y axis is the efficiency η , where (η_{sys}) is the system detection efficiency. On the X axis is the time course of the efficiency. The efficiency trajectory does not align with the real efficiency trajectory, and serves only for a visualization purpose.

Measurement and results

In this work, the recovery time of the detector is determined through an autocorrelation method based on a continuous wave laser source (a faint laser source). This technique has been previously employed by other research groups [19, 20]. The measurement was conducted with the setup shown in figure 4.3. The analog signals from the detector were directly guided with a SMA cable (SubMiniature version A) to a time tagger unit (Time Tagger 20) by Swabian instruments. The time tagger unit has self-adjustable trigger voltages, a device deadtime of 6ns and a maximal counting rate of 9MHz. This unit enabled the tagging of incoming signals with a time tag. Subsequently, the tags were used to process the time distances between all signals.

Histograms of the time distances between photons provide a distribution of the time distances, which yields an autocorrelation of the photon distances.

In order to determine the recovery time and analyze its dependencies on the bias current and the trigger voltage, the autocorrelation was measured for four different bias currents ($25\mu\text{A}$, $27\mu\text{A}$, $29\mu\text{A}$ and $31.2\mu\text{A}$) and trigger voltages from 300mV to 900mV in 100mV steps for a measurement period of 30s each. The results for a fixed bias current of $31.2\mu\text{A}$ are shown in figure 4.4(a) and for $25\mu\text{A}$ in 4.4(b). The other measurement results are presented in the appendix A.6.

The results of the autocorrelation show three major features. First, for low trigger voltages, the

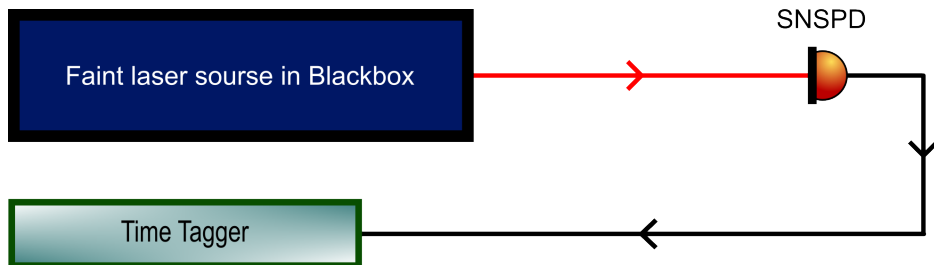


Figure 4.3: Experimental setup for measuring the recovery time. Optical setup of the "faint laser source in Black box" is depicted in 3.1.

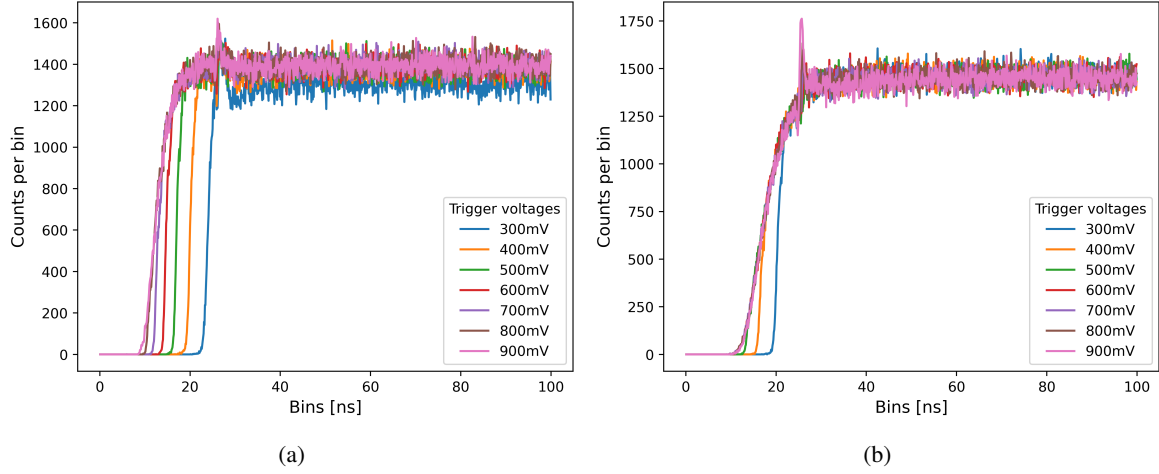


Figure 4.4: Autocorrelation of distances between two photon detection events for (a) $I_B = 31.2\mu A$ and (b) $I_B = 25\mu A$. Measurements were done with a input photon rate of 0.531 MHz. The X-axis represents the time distance between two signals in 1ns steps and the Y-axis the counts per bin.

dead time is longer and decrease for increasing trigger voltages. This is true for both, the lower and higher bias current. The reason for this behavior can be explained best by looking at an exemplary analog signal (see figure 4.5) of two consequent pulses. In figure 4.5 one can see the peaks of two consecutive detection signals, where the second pulse starts ($\approx 25\text{ns}$) before the falling edge of the first pulse ends. Physically, that means, that before the first signal spike has fully decayed a second photon, already hit the detector, got detected and produced a second spike.

If the trigger is *below* a certain threshold Tresh^* the time tagger will count this signal as one count, since the second pulse came when the remaining voltage of the wire was still *above* Tresh^* . If the trigger is *above* Tresh^* both pulses will be counted. This allows counting of successive events with smaller time delay between them and therefore reduces the perceived recovery time. Due to time constraints, no further investigation was done to record double pulses with a distance below ($\approx 25\text{ns}$).

Second, for the lower bias current ($26\mu A$), the rising curves for each trigger voltage converge earlier in comparison to the bias current of $31.2 \mu A$. At the bias current of $31.2 \mu A$, the four different curves remain distinct until they reach their peak. This can be attributed to the differing pulse heights, dependent on the bias current. According to Ohm's law, for the same resistivity, a lower bias current corresponds to lower voltage pulses and vice versa. Due to the lower pulse, the regime, where pulses can be resolved by a trigger voltage of 600mV but not 500mV becomes smaller. The different pulse heights can also be verified by the recorded analog signals shown in figure: 4.11.

The third interesting feature is the peak at $24\text{ns}-27\text{ns}$ for $31.2\mu A$ in all autocorrelation measurements as can be seen in figure 4.4(a) and 4.4(b). This behavior can be understood by taking into account that the bias current needs a finite amount of time to reach its target value once the superconductivity is restored and will also overshoot a bit after reaching the target value. A sketch of the expected behavior is shown in figure 4.6.

The current during the nanowire recovery does not proceed directly and precisely to the bias current. Instead, it oscillates for a brief period and then rapidly reaches equilibrium. If the target bias current is close to the critical current, the overshooting might cause a breaking of the superconductivity leading

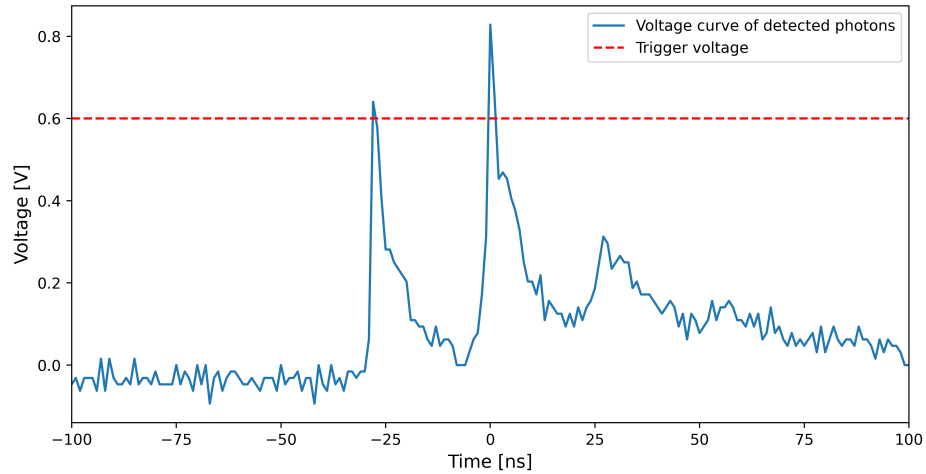


Figure 4.5: Analog signal of three consecutive pulses recorded with an oscilloscope with trigger at 600mV. Detector was set up to a bias current of $31.2\mu\text{A}$ and the faint laser source was attenuated down to 0.531 MHz. The time resolution of the oscilloscope was 500MHz.

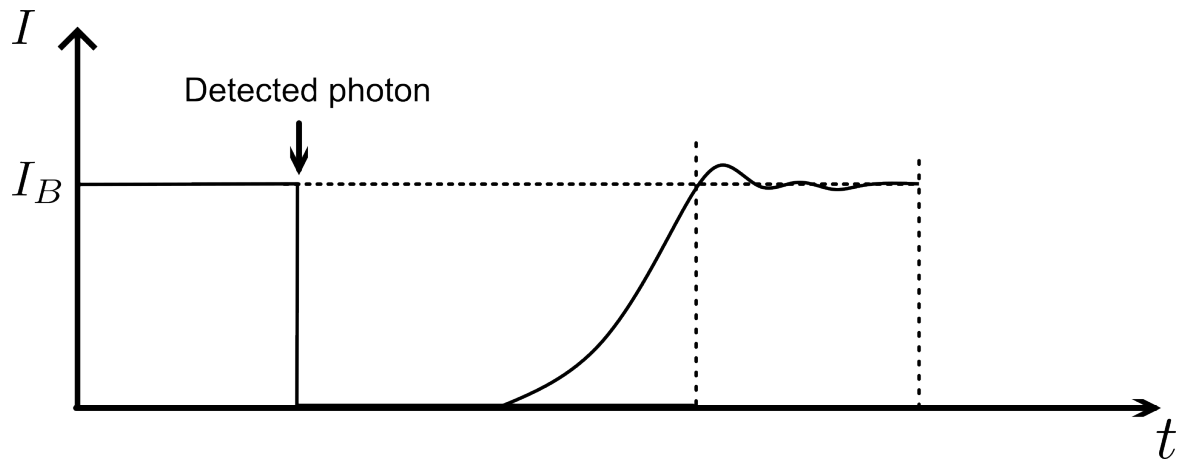


Figure 4.6: A sketch of the assumed bias current behaviour. Once the bias current has been reached, the current undergoes a brief oscillation before stabilising at the bias current level.

to a time correlated increase in the dark count rate (seen in figure 4.1).

A reasonable working point would be at a bias current of $31.2\mu\text{A}$ and a trigger voltage of 600mV , since it yields the best compromise between a short recovery time and a low additional oscillation signal as discussed above.

Finally, the calculation of the recovery time (τ_{rec}) is done by measuring 10 times the autocorrelation for this configuration. Afterwards, analogue bin values are averaged and the error is calculated by the standard deviation.

To calculate the recovery time, first the bin counts from 28ns till the end of the measurement period were averaged. The time 28ns is chosen as the starting point because from this point a constant curve, hence maximal detection efficiency, is assumable (saturation value). Based on this saturation value a 05% , 50% and 90% bin count threshold is calculated. The threshold is then used to define the dead time τ_{dead} as the time, where the detector is reached 05% of the saturation value. Furthermore, the reset time τ_{reset} is defined as the time from 05% till 90% of the saturation value. The calculated points are visualized in figure 4.7. The recovery time is then calculated by the sum of the dead and reset time $\tau_{\text{rec}} = \tau_{\text{dead}} + \tau_{\text{reset}}$. Errors are calculated by using the mean root square of the corresponding standard deviation of the dead and reset time.

The final results are $\tau_{\text{rec}}^{90\%} = (17.156 \pm 0.0445)\text{ns}$, where $\tau_d = (13.950 \pm 0.050)\text{ns}$ is the dead time and $\tau_r = (3.206 \pm 0.447)\text{ns}$ the reset time. Moreover, the time the detector is back at efficiency of $\eta_{\text{sde}} = 50\%$ is $\tau^{50\%} = (14.900 \pm 0.0816)\text{ns}$. The dead time also define the maximal possible count rate of $\mathcal{R}_{\text{max}} = \frac{1}{\tau_d} = (71.68 \pm 0.25)\text{MHz}$.

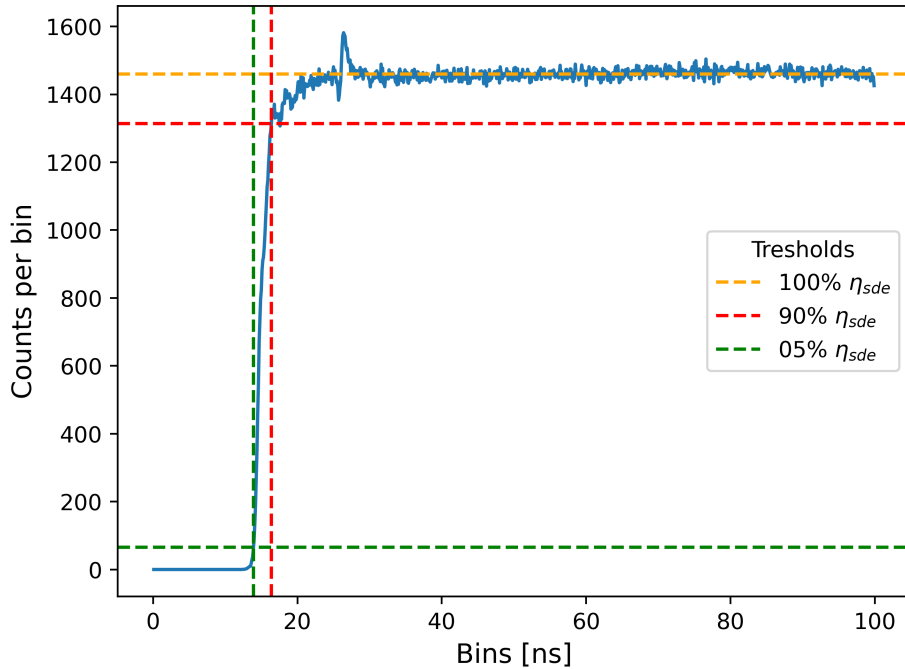


Figure 4.7: Autocorrelation of averaged distances between two photon detection events for $I_B = 31.2\mu\text{A}$ and 600mV. The X-axis represents the time distance between two signals in 1ns steps and the Y-axis the counts per bin. H- and v-lines indicate the dead-; reset- and recovery time.

4.3 Efficiency

Efficiency is a way of measuring how likely a process is to happen. There are three types of efficiencies that describe independent loss processes in single photon detection, the coupling efficiency (η_C), the absorption efficiency (η_A) and the registration efficiency (η_R). The graph 4.8 shows schematically where the different losses in the detection process appear. When a photon is sent to a detector via an optical fibre, not all photons can be coupled into the fibre. The probability of coupling is the so called *coupling efficiency*. When photons hit the detector, there is always a probability that the photon will not be absorbed by the detector. This is due to material and symmetry properties in the design of the superconducting nanowire [15]. This is described by the *absorption efficiency*. Finally, there is always a probability that the photon will not be registered by the measuring electronics. This is expressed with the *registration efficiency*.

In literature, these terms are summarized in two general efficiency terms: the device detection efficiency ($\eta_{dde} = \eta_A \cdot \eta_R$) and the system detection efficiency ($\eta_{sde} = \eta_A \cdot \eta_R \cdot \eta_K$) [8, 15]. The device detection efficiency η_{dde} corresponds to the efficiency of the device itself and neglects coupling inefficiencies. This gives an idealized upper bound to the achievable efficiency. For perfect optical coupling, the device detection efficiency is equal to the system detection efficiency ($\eta_{dde} = \eta_{sde}$). The system detection efficiency η_{sde} takes the coupling losses to the optical fibre into account. This is the case if the detector is connected to a fibre, as the device properties or the experiment does not allow photon detection in a free environment.

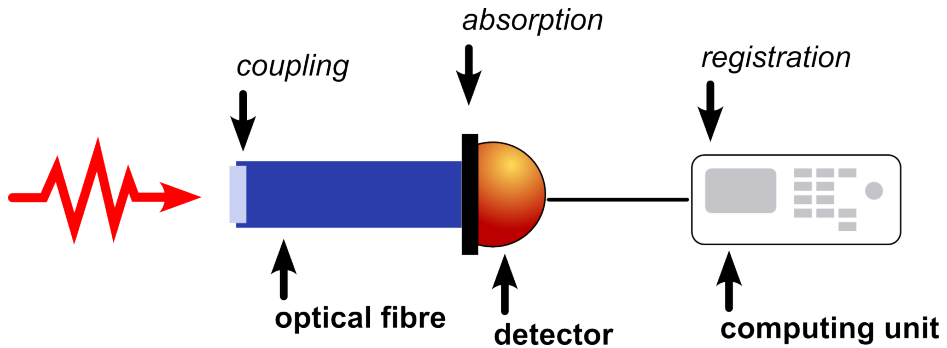


Figure 4.8: Sketch of the components in the detector setup where photonlosses appear and consequently a probability (η_K , η_A or η_R) has to be considered.

Measurement and results

In the given setup, only the system detection efficiency η_{sde} is measured, because the detector is already prebuild with a fixed coupling to a fibre [10]. This internal fibre is connected to a single mode fibre to fibre port for the connection type FC/PC. The connector type FC/PC is used in order to maintain higher efficiency coupling [10]. Through this port, one can connect the detector with an external optical fibre and send photons from the experiment to the detector.

The system detection efficiency η_{sde} depends on the photon polarization (see section 4.3), the applied bias current, the chosen trigger voltage (see section 4.3) and the photon rate send to the detector (see section 4.3). These dependencies will be investigated and the system detection efficiency will be determined. Each measurement was done with the optimized faint laser source setup, as discussed in section 3.

Polarization dependency

The measurements were done in a specific order since the conclusions drawn for certain measurements influence the preceding measurements. It is first necessary to align the polarization of the laser light with the slow axis of the fibre connected to the output port of the detector. According to the manual the coupled light needs to be polarized along the slow axis of the fibre [10]. This is explained by the fact that the absorption efficiency (η_A) is maximized when the light is polarized parallel to the superconducting nanowire of the detector as explained in section 2.

A combination of a quarter-wave plate λ_4 and a half-wave plate λ_4 is used to alter the polarization of the input laser light. The quarter-wave plate is used to pre compensate the stress induced birefringence of the fiber input while the half-wave plate is used to rotate the linear input polarization. The measurement of the polarization was done with the polarization analyzer SK010PA by Schäfter + Kirchhoff. Furthermore, the laser power input was set to $511.1 \mu\text{V}$, corresponding to a photon rate of 2.006 PHz, and attenuated by three ND filters with a total OD of (9.574 ± 0.105) , in order to make sure the condition of $N(T) \cdot \eta \ll 1$ as discussed in section 3.1. Different polarization angles for measuring the count rate of the detector are then realized by rotating the half-wave plate while the quarter wave plate is kept in its position.

By rotating the half-wave plate in $(10 \pm 2)\text{deg}$ steps, the polarization axis was rotated relative to the slow axis of the fibre. With this, it was possible to find the angle configuration where the maximum of

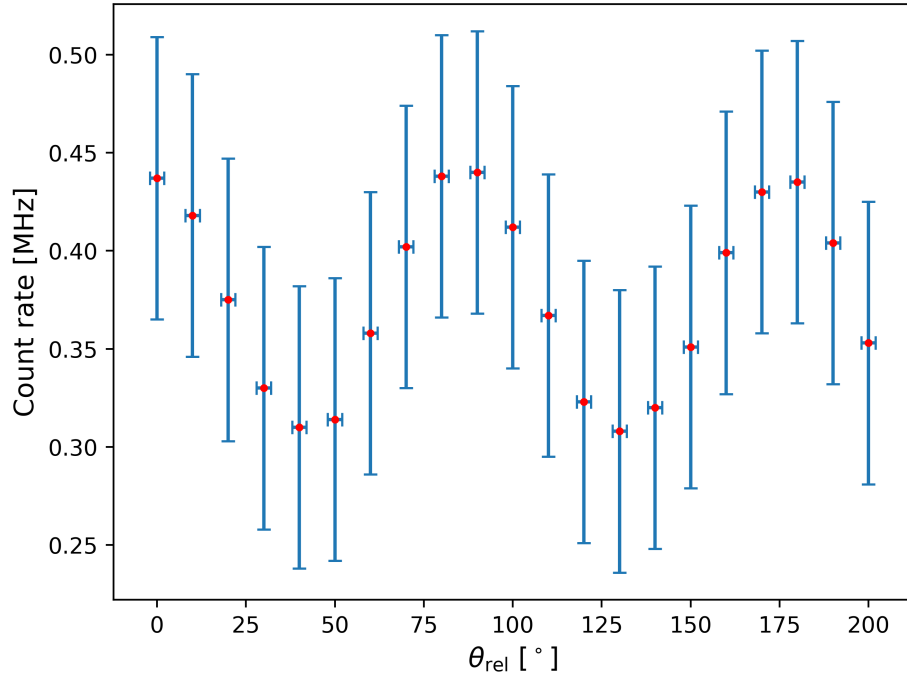


Figure 4.9: On the X-axis the relative angle to the slow axis is depicted with an estimated error of 2° . The Y-axis shows the angle dependent count rates. Countrate errors are listed in table A.4 and calculated according to the calculation mentioned in A.2.

light was coupled to the slow axis of the fibre. This is important since measuring subsequent efficiency measurements aligned to a different axis would put a systematic downshift on the true efficiency of the detector.

In the figures 4.9 the count rates are depicted. For preceding measurements the polarization was aligned to the relative angle of $(0 \pm 2)^\circ$, where the maximum count rate was reached.

Trigger voltage and bias current dependency

In a second measurement the trigger voltage and bias current dependency was investigated for different count rates. For this measurement a different power as input was used because the power drifted over time and could not be reproduced to the power level used in the polarization alignment. The new power level was set to $518.1 \mu\text{V}$, corresponding to a photon rate of 2.034 PHz . Furthermore, the ND filters were used for attenuation to reach different count rates in the MHz regime.

In order to investigate the trigger voltage and bias current dependency the bias current was swept from 0 to $35 \mu\text{A}$ in $0.1 \mu\text{A}$ steps and events within 1s integration time were counted.

In figure 4.10(a) and 4.10(b) one can see that at a lower trigger voltage of 300 mV the count rate oscillates a bit. This likely corresponds to the increased dark count rates, due to the overshoot of the critical current, as explained in figure 4.6.

Furthermore, one can see that in the lower bias current regime the count rates are higher for the lower trigger voltages. This corresponds to the detection of lower voltage pulses. Another behaviour is the constant count rate, beginning at $I_{\text{Bias}} \approx 20 \mu\text{A}$. A constant count rate is reached independent of

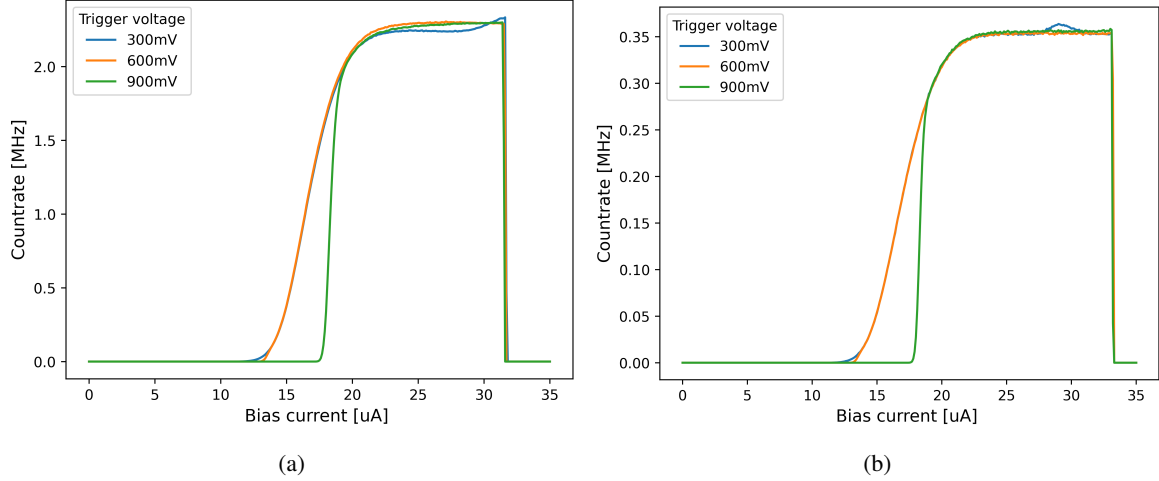


Figure 4.10: Count rates for different bias currents and trigger voltages. The count rates are measured for a trigger voltage of 300mV, 600mV and 900mV. (a) shows the measured count rates for an input count rate of 2.45MHz and (b) for 0.39MHz. The curves for a trigger voltage of 300mV and 600mV are laying on each other and are not distinguishable in the lower bias current regions.

the trigger voltage (except for the light fluctuation at a trigger voltage of 300mV). At the end of the curve, for the higher count rate (a) the counting of the detector drops at a bias current of $I_{Bias} \approx 32\mu A$ and for the lower count rates (b) at $I_{Bias} \approx 34\mu A$. One can assume that the critical current is reached earlier when more photons are send to the detector, because the nanowire is not able to recover that fast enough. Overall, one can also conclude that the behaviour of the count rates does not change significantly for the trigger voltages of 600mV and 900mV.

An interesting observation is that if the count rate reached a certain high amount (here at 547.546KHz), the produced voltage peak is decreasing. This behaviour counteracts the behaviour of a rising voltage peak, when the bias current is increased. This can be seen in recordings of voltage pulses with the same bias current and trigger voltage *but different count rates* (shown in figure 4.11). Moreover, if several photons are detected in a short time period, the voltage amplitude of successive pulses are fluctuating. This is observable in the comparison in the three consecutive pulses of the orange curve in figure ??.

This behaviour can also be seen in figure A.5(a) along the lower count rates for higher trigger voltages in the appendix A.5.

One possible explanation for this phenomenon is that the hotspot in the nanowire has not been entirely dissipated, resulting in incomplete restoration of the initial superconductivity. Therefore, successive triggered events have not the same pulse amplitude.

Accordingly, the optimal working point with regard to bias current and trigger voltage is dependent upon the photon rate being transmitted to the detector. A midpoint trigger voltage of 600 mV is reasonable when measuring with a count rate in the 300 kHz regime. For higher count rates, a reduction in the trigger voltage may be appropriate. However, this may result in an increased risk of detecting noise signals, such as cable back reflection seen in ??.

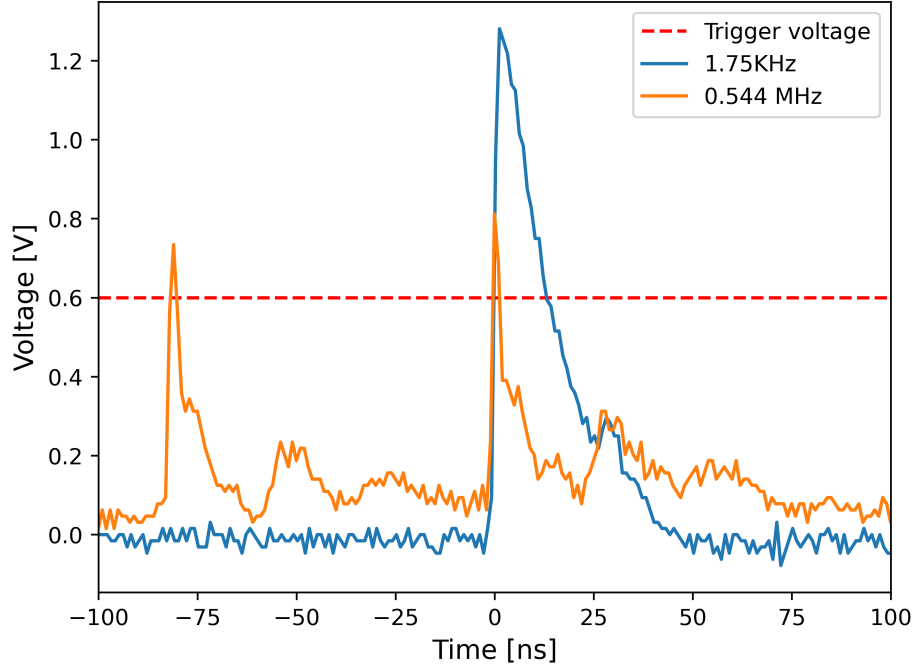


Figure 4.11: Analog voltage pulse signals for the count rates 0.544MHz (orange curve) and 1.771KHz (blue curve). In both recordings the same bias current $I_b = 31.2\mu\text{A}$ and trigger voltage 600mV is used. At $\approx 26\text{ns}$ a minor peak on both descendings curves is visible. This may be attributed to back reflection in the cable. Furthermore, signals at higher count rates are followed by more underground noise. This can be seen at the underground offset of the orange curve.

Input photon rate dependency

Finally, efficiency measurements for different count rates were done, to determine the bandwidth where events are detected with the constant maximum efficiency.

The count rates were varied by using different combinations of ND filters. With this, six different count rates (2.446MHz, 0.531MHz, 0.388MHz, 0.0674MHz, 12.300KHz, 1.800KHz) were generated.

To avoid the oscillation of count rates near the critical current as seen in the blue curve in figure 4.10(a) and 4.10(b) a trigger voltage of 600mV is used. Further, the bias current was set to $31.2\mu\text{A}$, since it yields the best recovery time as discussed in section 4.2.

However, with this operating bias current it is not possible to measure higher count rates than 2.45MHz (OD = 8.92), due to an earlier breakdown of counting corresponding to the failing recovery of the superconducting nanowire.

For each of the 6 input count rates the detected count rate was measured for 30s with an integration time of 1 second. This measurement was repeated 5 times. Afterwards, the system detection efficiency η_{sde} was calculated by the formula $\eta_{\text{sde}} = \frac{\mathcal{R}_{\text{mean}}}{\mathcal{R}'_{\text{incident}}} \cdot 100$. Where $\mathcal{R}_{\text{mean}}$ are the averaged count rate of the 5 measurements and $\mathcal{R}'_{\text{incident}}$ is the incident photon rate. $\mathcal{R}'_{\text{incident}}$ was calculated via the OD of the ND filters and the photon number per second of the initial laser power $\mathcal{R}_{\text{incident}'} = \Phi \cdot 10^{-\text{OD}}$. The resulting 6 efficiency values are plotted vs the input count rates in figure 4.12.

In figure 4.12 one can see a rather constant trend of η_{sde} . No significant decrease in efficiency can

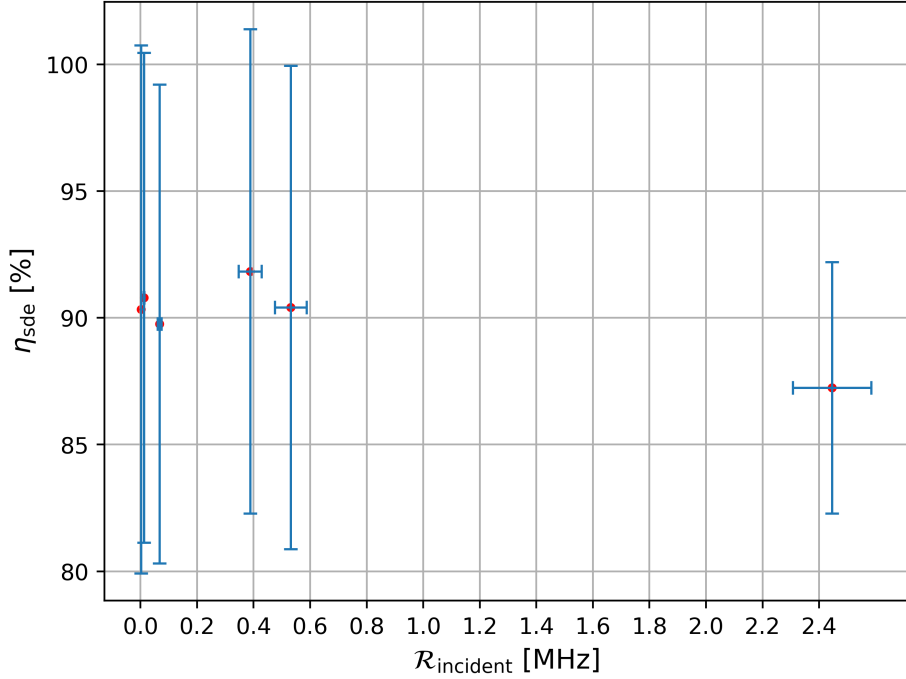


Figure 4.12: System detection efficiency appears in a range between $(87.242 \pm 4.955)\%$ and $(91.834 \pm 9.559)\%$. Errors are calculated according to A.2 and due to the high uncertainty in the OD calculation unphysical values of over $\eta_{\text{sde}} = 100\%$ are included in the error range. Calculated values are listed in table A.5.

be observed. In order to investigate the behaviour further, measurements were done for two higher count rates (67.363MHz and 9.575MHz).

From the count rates of a bias sweep measurement (seen in figure 4.13(a)), the point with the highest count rates was selected. With these additional values, the η_{sde} was again plotted against the count rate (log scale) as shown in figure 4.13(b).

In figure 4.13(a) one can clearly see two different behaviours. First, for higher count rates the maximum bias current that the detector can handle is reached earlier and no constant count rate is reached. This dynamic follows from the fact that the detector is not able to recover in time, when the count rate is too high. Hence, the critical temperature is reached earlier and does recover again. As result the detector shuts down. This makes the counting process highly unstable and unreliable, because one wants to measure with a high but also stable count rate. This is not the case for the count rate of 67.363MHz. No stable count rate is reached, and the highest count rate is close to the edge of the breakdown, which is not desirable.

Secondly, the system detection efficiency η_{sde} sinks for higher count rates. This can be explained by the fact that at certain count rate, the average photon per dead time unit is above 1, which directly corresponds to a decrease in the absorption efficiency η_A .

Finally, the measurements in figure 4.13(b) show a constant efficiency course for count rates lower than 9.575MHz. Then, the efficiency decreases for higher count rates. Due to time constraints, no further measurements were done to investigate the efficiency behaviour for other count rates. All results are listed in table A.5. All system detection efficiency values appear in a range between

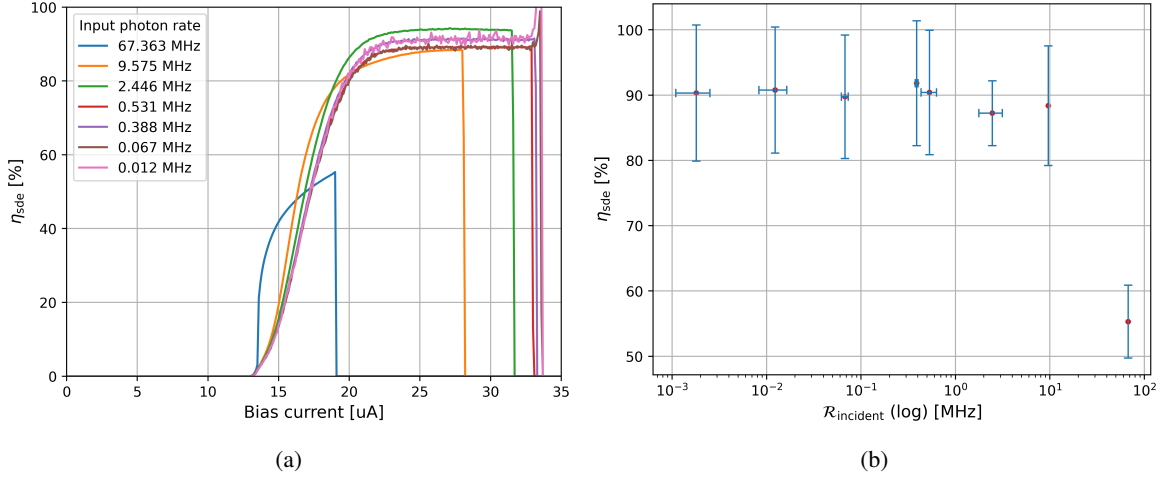


Figure 4.13: (a) Curves of system detection efficiency for different bias current. The curve for 0.39MHz was left out because the high relative fluctuations made the other cuvers unreadable. The raising edges at the end of the curve are due to the rising noise, as already seen in 4.1. In (b) curve of system detection efficiency for two further higher count rates plotted on a logarithmic X - axis to emphasize the efficiency bandwidth. For better visualizatlon, the errors for R_{incident} were scaled down by a factor of 10.

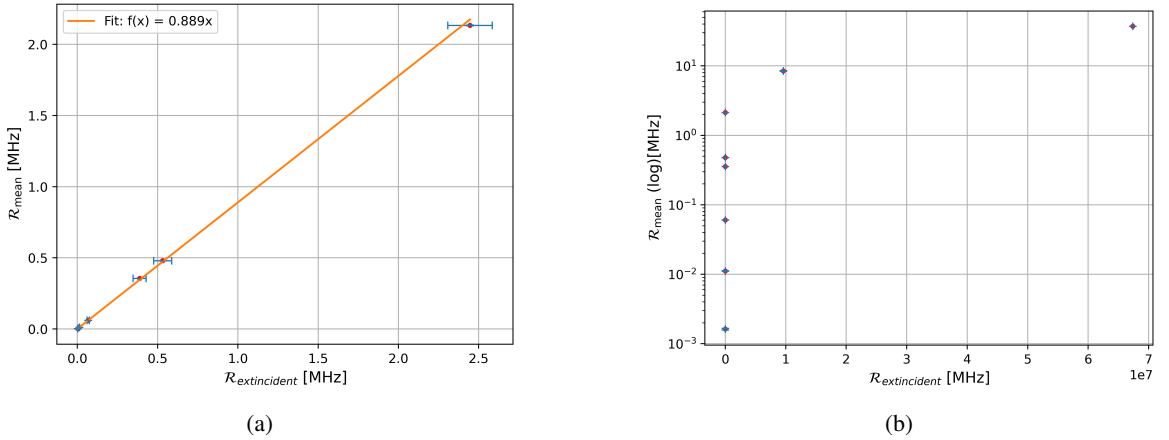


Figure 4.14: (a) Shows the linear Orthogonal Distance Regression (ODR) fit of R'_{incident} against R_{mean} . The fit is done with SciPy and considers the uncertainties of x- and y. The fit yields a slope of $m = 0.893 \pm 0.008$ with $\chi^2 = 705.610$. In (b) the extented count rate (log scale) is plotted against the extended incident photon rate.

$$\eta_{\text{sde}} = (87.242 \pm 4.955)\% \text{ for a count rate of } 2.446 \text{ MHz at a count rate of } 0.3876 \text{ MHz.}$$

These results are in agreement with the specification of the company, which measured a system detection efficiency of $87 \pm 3\%$ for a incident count rate of 395 KHz [6]. However, the results bring two caviats. First, the error of η_{sde} is very large. This lowers the significance of the results. Second, the error of R'_{incident} are correlated with the error of η_{sde} . This dependent errors have the effect of distorting the presentation of the results.

In order to compensate this effect, R'_{incident} was plotted against R_{mean} and a linear orthogonal distance regression (ODR) with SciPy was done in order to consider the x- and y-errors. The

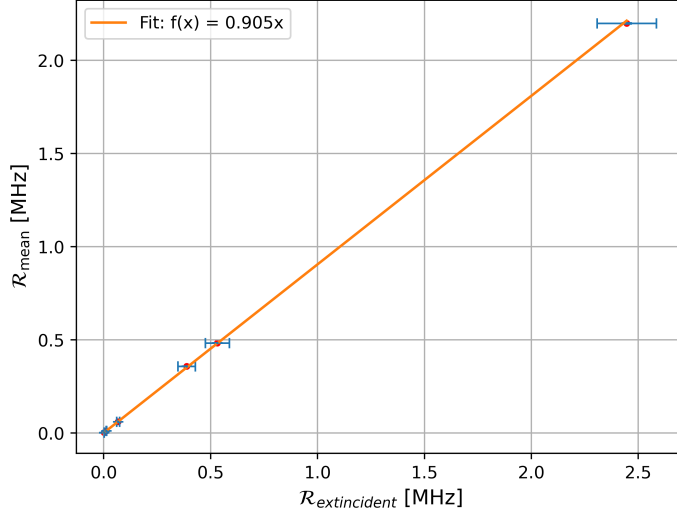


Figure 4.15: Shows the linear ODR fit of $\mathcal{R}'_{\text{incident}}$ against $\mathcal{R}_{\text{mean}}^{\text{corrected}}$. The fit is done with SciPy and considers the uncertainties of x- and y. The fit yields a slope of $m = 0.900 \pm 0.002$ with $\chi^2 = 0.000187$.

regression was done, because it is assumed that η_{sde} stays constant, hence the relation scales linearly with $\mathcal{R}_{\text{mean}} \leq 2.446 \text{ MHz}$. The results of the ODR fit are shown in figure 4.14(a). The fit yields a slope of 0.893 ± 0.008 with $\chi^2 = 705.610$, corresponding to efficiency values of $\eta_{\text{sde}} = (89.30 \pm 0.78)\%$ for an incident photon rate below $\mathcal{R}'_{\text{incident}} \leq 2.446 \text{ MHz}$.

In addition to the system detection efficiency, in figure 4.14(b) the count rate is plotted against the incident photon rate for the extended count rates of 67.363MHz and 9.575MHz. This plot shows the same behaviour as figure 4.13(b), but displayed with $\mathcal{R}_{\text{mean}}$ against $\mathcal{R}'_{\text{incident}}$ resulting in smaller errors in the presentation. Moreover, one can see in this plot, that $\mathcal{R}_{\text{mean}}$ would converge for high $\mathcal{R}'_{\text{incident}}$ to the calculated maximum count rate of $\mathcal{R}_{\text{max}} = (71.68 \pm 0.25) \text{ MHz}$.

Finally, one has to consider the correction of $\mathcal{R}_{\text{mean}}$. The count rate the detector is showing us, are not only limited by the system detection efficiency η_{sde} but also by our faint laser source. It means, considering poisson distributed photons (for $N(T) \cdot \eta \ll 1$) there is always the probability that a certain amount of photons is timely spaced by less than the dead time of the detector. As described 3.1 the true count rate of our laser source is then given by equation (3.4). Redoing the linear orthogonal distance regression (ODR) with the corrected count rates (seen in figure 4.15), gives a slope of $m = 0.905 \pm 0.004$ with $\chi^2 = 176.014$ corresponding to a system detection efficiency of $\eta_{\text{sde}} = (90.47 \pm 0.36)\%$. The value $\eta_{\text{sde}} = (90.47 \pm 0.36)\%$ is not in agreement with the company specification of $87 \pm 3\%$ [6]. However, one has to consider, that the specifications of the company are based on a laser source with a wavelength of 785nm [6]. Since the used laser has wavelength of 780nm and the efficiency also depends on the wavelength [8], all values are not exact comparable. Nevertheless, this value is used as the final result for the system detection efficiency $\eta_{\text{sde}}^{\text{ch1}}$ of the first channel of the SNSPD since it comes very close to the given specification [6].

4.4 Summary of the results

These final results (listed in table 4.1) yield the measured characteristics of channel 1 of the SNSPD. They are listed in the column "Measurement" next to the given specification in column "Single Quantum" [6]. The column "Agreement" lists, if the measured value is in agreement with the specification.

Characteristics	Single Quantum	Measurement	Agreement
$\eta_{\text{sde}}^{\text{ch1}} [\%]$	$(87 \pm 3)\%$	$(90.47 \pm 0.36)\%$	Yes
DCR [Hz]	$< 5 \text{ Hz}$	$(1.40 \pm 1.36)\text{Hz}$	Yes
τ_{recovery} [ns]	-	$(17.156 \pm 0.045)\text{ns}$	-
τ_{dead} [ns]	-	$(13.950 \pm 0.050)\text{ns}$	-
Maximum count rate [MHz]	-	$(71.68 \pm 0.25)\text{MHz}$	-
Timing jitter [ps]	17.52ps	-	-
Figure of merit H	-	3.628×10^{10}	-

Table 4.1: Final measurement results of the SNSPD Characterization of Channel 1. Missing or not calculatable values are marked with a "-".

For the recovery time, dead time and maximum count rate no specification was available, however the measurement were reasonably close to other specification data of the company for detectors in similar wavelength range [21]. Additionally, the timing jitter Δt measured by the company v[6] and a figure of merit $H = \frac{\eta_{\text{sde}}}{DCR\Delta t}$ according to [15] is calculated. This can be used as compact comparison value for the quality of the detector, where higher H values indicate better detectors.

CHAPTER 5

Summary and Outlook

In this thesis, both the quantitative verification of the company's specification data for one channel of the SNSPD and the analysis of the dependencies on the bias current, trigger voltage, polarization and count rate of the SNSPD were successfully completed. The results of the system detection efficiency, dark count rate, recovery time, dead time and maximum count rate are summarized in table 4.1 and compared with the specification available [6].

The basis for the characterization was a faint laser source setup. This served as a source for measuring single photons and made measurements of SNSPD characteristics possible. For realizing a faint laser source set up a laser with a wavelength of $\lambda = 780\text{nm}$ was used and attenuated by ar ND filters. For the precise measurement of the OD values of the filters, a calibration of the filters was done in two ways to consider statistical and systematic errors. Moreover, the faint laser source set up was operated in a self-build optical enclosure (black box) to avoid environmental light coupling into the fibre.

After the setup was built, first Dark count measurements were performed. Different settings were investigated 4.1 to find the optimal settings for the lowest Dark count rate. The lowest dark count rate was achieved by operating the faint laser source in the black box and coating an aluminium foil around the optical fibre connecting it to the SNSPD. A dark count rate of $DCR_{31.2\mu\text{A}} = (1.40 \pm 1.36)\text{Hz}$ was achieved and yields the same low values as for the case, where the detector has no connection to the experiment. Afterwards the recovery, dead and reset time was determined with a time tagger unit (Time Tagger 20) by Swabian instruments. With a common used autocorrelation evaluation [19, 20] of the time distances between detected photons, the three times were determined. The results yield for the bias current of $I_B = 31.2\mu\text{A}$ and a trigger voltage of 600mV the following values:

- Recovery time: $\tau_{\text{rec}} = (17.156 \pm 0.0445)\text{ns}$
- Dead time: $t_{\text{dead}} = (13.950 \pm 0.050)\text{ns}$
- Reset time: $t_{\text{reset}} = (3.206 \pm 0.447)\text{ns}$

The results are in the range of the values of the companies specification data [6] and would make the detection of single photons with count rate up to $(71.68 \pm 0.25)\text{MHz}$ possible. Furthermore, in the evaluation of the recovery time three interesting features were observed. First, for low trigger voltages, the dead time is longer and shortens for increasing trigger voltage up to a trigger voltage of 800mV

(seen in figure 4.4(a)). For higher voltages the dead time stays constant. Second, for lower bias current ($26\mu\text{A}$), the rising curves for each trigger voltage converge earlier in comparison to the bias current of $31.2\mu\text{A}$. Moreover, the curve back to full efficiency is steeper for the higher bias current $31.2\mu\text{A}$. The third interesting feature is the additional "counts per bin" peak at (24-27 ns) for all trigger voltages and bias currents (seen in figures 4.4(b), 4.4(a) and 4.2). This peak might be explained by a brief overshooting of the bias current and therefore a resulting rise in dark counts (as seen in figure 4.1) due to short time excess of the critical current.

Finally, the system detection efficiency was measured. First the polarization dependency of the setup was analyzed and the optimal settings were set in order to achieve the highest efficiency (shown in figure 4.9). After this, the trigger voltage and bias current dependency were evaluated. It was found that the efficiency is stable and independent of the trigger voltage, for an input count rate up to 2.446MHz (shown in figure 4.10(a) and 4.10(b)). At the end, the relation to the count rate was investigated and a expected downward trend for higher count rates was observed and a constant system detection efficiency in the range between $(89.833 \pm 9.447)\%$ and $(92.292 \pm 9.550)\%$ for count rates up to 9.575 MHz was found 4.13(b).

Next steps would be the investigations and characterizations of the other seven available channels. Further, a standard procedure can be developed for accelerating the characterization process. Moreover, when the characterization of all channels is finished, the SNSPD can be used to measure in a Hanbury Brown and Twiss set up. This set up can measure the second order correlation function $g^{(2)}(\tau)$ of the faint laser source and confirm the characteristic constant curve for coherent light sources [22]. Finally, the SNSPD can be used in the HQO experiment for measurements of strong nonlinearities in Rydberg physics.

APPENDIX A

Appendix

A.1 Set up and elements

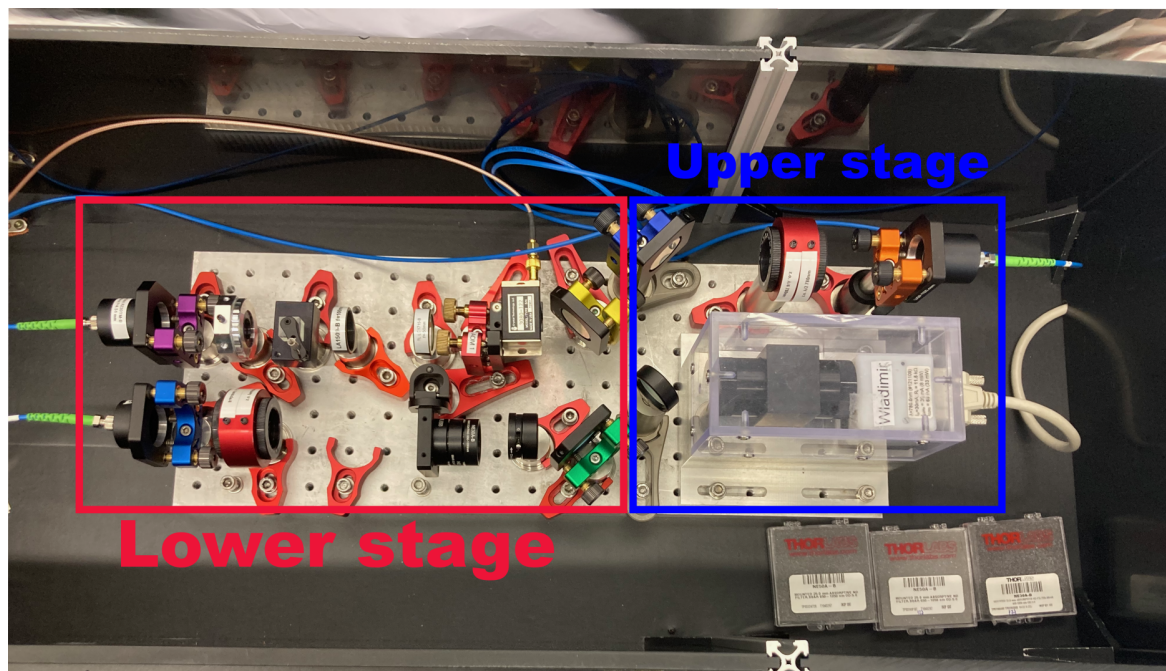


Figure A.1: Set up for attenuation of a 780nm laser source from the Russian company Vitawave

Appendix A Appendix

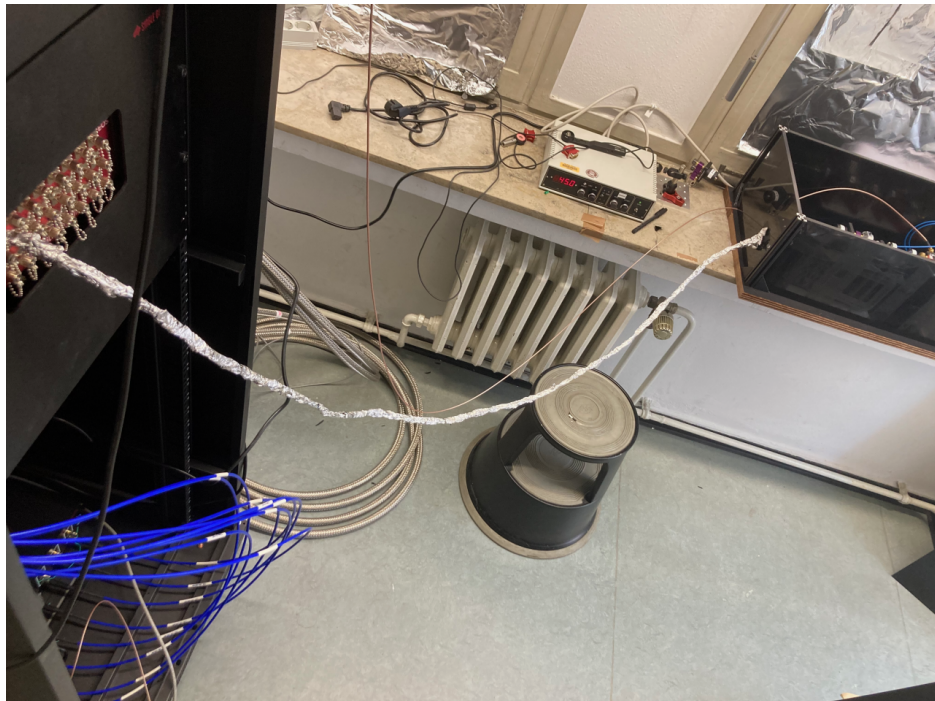


Figure A.2: Fibre connection to the detector from the black box. The optical fibre is going through a whole in the black box and is connected to the outcoupler of the faint laser source.



Figure A.3: Picture of the self build optical enclosure (black box) from the outside.



Figure A.4: Picture of the self build optical enclosure (black box) from the inside

A.2 Neutral density filter calibration - Error calculation

To calculate the OD value of the ND Filters, we have to consider the statistical error from the transmission value and the systematic error, we get from measuring the OD with two methods, as explained in 3.2.

We first consider the statistical error from the transmission value. The transmission is given by:

$$T = \frac{P_{ND}}{P} \quad (\text{A.1})$$

Where P is the power detected by the power metre without the ND filter and P_{ND} is the power we measured with applied ND filter.

For the Error calculation the following considerations are done:

First, for both P and P_{ND} the measurement uncertainty of the photodiode from the photodiode is always 3% of the measured value [23]. Since this uncertainty does not affect the overall relation between the two measurements it does not contribute to the error calculation. However, the measurement uncertainty from reading the value from the Powermeter contributes to both, P and P_{ND} , since reading the value from the powermeter provides always a different error because the last displayed order of magnitude of the displayed result on the powermeter fluctuates.

Further, regarding ΔP it is also important to mention that after each ND filter change, the coupling was readjusted to the maximal vale. However, after the ND filter was removed it was not possible to get to the same initial value. Therefore, we always have different power values we compare, though the filtering process was done always with the same fixed laser power setting. Based on this, P is the mean value of all initial values was taken and for the error the standard deviation was calculated.

Appendix A Appendix

Due to this we have also to consider an *additional error source* ΔP^{STD} from the fiber coupling and optimization in ΔP .

Important: This only applies for the first measurement method because we adjust there our fiber coupling. In the second measurement we have a stable P because there, the fiber coupling was not adjusted, once the maximum was reached.

So, ΔP for the first measurement method is calculated as follows:

$$\Delta P = \sqrt{(\Delta P_{\text{Read off}})^2 + (\Delta P_{\text{STD}})^2} \quad (\text{A.2})$$

For P_{ND} applies:

$$P_{\text{ND}} = P \cdot 10^{-\text{OD}} \quad (\text{A.3})$$

The corresponding error is $\Delta P = 0.03 \cdot P$ (uncertainty of the photodiode) and hence the total error for the power after the ND filter is calculated as follows:

$$\Leftrightarrow \Delta P_{\text{ND}} = \sqrt{(\Delta P \cdot 10^{-\text{OD}})^2 + (P \cdot \log(10) \cdot \Delta \text{OD})^2} \quad (\text{A.4})$$

An additional error from reading off the count rate (hence, the corresponding Power) from the computer screen was also considered, since measurement with the power metre was not able. However, because the fluctuating rate of the count rate was in the order of a few Hz, it was neglected for the final error calculation.

As result, we get the following error for the transmission rate:

$$\Delta T_{\text{stat}} = \sqrt{\left(\frac{\Delta P_{\text{ND}}}{P}\right)^2 + \left(\frac{\Delta P P_{\text{ND}}}{P^2}\right)^2} \quad (\text{A.5})$$

Further for calculating the total transmission value and its error, we have to include the measurements and errors for the second method. Here, we have stable power P because the fiber coupling was not adjusted, once the maximum was reached. The transmission error for the second method is also calculated the same way as above:

$$\Delta T = \sqrt{\left(\frac{\Delta P_{\text{ND}}}{P}\right)^2 + \left(\frac{\Delta P P_{\text{ND}}}{P^2}\right)^2} \quad (\text{A.6})$$

but both values ΔP_{ND} and ΔP are estimated by the read off error of the powermeter.

With booth transmission values, the total transmission value and its total error (systematic and statistical) can be calculated as follows:

Appendix A Appendix

$$T_{\text{total}} = \frac{T_{\text{stat}} + T_{\text{systematic}}}{2} \quad (\text{A.7})$$

$$\Delta T_{\text{total}} = \sqrt{\Delta T_{\text{stat}}^2 + \Delta T_{\text{systematic}}^2} \quad (\text{A.8})$$

Since, we do not know from which method the results are closer to the real OD value, we take the mean value of both values.

Continuing with the calculation of the OD value, we have according to [24] the relation: $\text{OD} = \log(\frac{1}{T})$. From this, we can calculate the error for the OD: $\Delta \text{OD} = \frac{\Delta T}{\ln(10) \cdot T}$

Below are the tables with the calculated values and results for the first and second method, as well for the combined results which lastly provide the final OD values used for the calculations:

ID	P_{before} [W]	\bar{P}_{before} [W]	Std P_{before} [W]	ΔP_{before} [W]	P_{after} [W]	P_{measured} [W]	T_{Measured}	$\Delta T_{\text{Measured}}$	OD _{Expected}	OD _{measured}	$\Delta \text{OD}_{\text{measured}}$	Deviation (%)
TP03337667	5.117×10^{-4}	5.257×10^{-4}	1.011×10^{-5}	1.031×10^{-5}	7.884×10^{-5}	1.500×10^{-1}	3.104×10^{-3}	1.00	0.8240	0.0090	17.60	
TP03337667 (2)	5.300×10^{-4}	5.257×10^{-4}	1.011×10^{-5}	1.031×10^{-5}	8.024×10^{-5}	1.526×10^{-1}	2.944×10^{-3}	1.00	0.8163	0.0084	18.37	
TP03366490	5.130×10^{-4}	5.257×10^{-4}	1.011×10^{-5}	1.031×10^{-5}	4.521×10^{-6}	8.600×10^{-3}	1.813×10^{-4}	3.00	2.0655	0.0092	93.45	
TP03366490 (2)	5.300×10^{-4}	5.257×10^{-4}	1.011×10^{-5}	1.031×10^{-5}	4.450×10^{-6}	8.465×10^{-3}	1.676×10^{-4}	3.00	2.0724	0.0086	92.76	
TP03275234	5.260×10^{-4}	5.257×10^{-4}	1.011×10^{-5}	1.031×10^{-5}	5.550×10^{-7}	1.056×10^{-3}	4.328×10^{-5}	4.00	2.9764	0.0178	102.36	
TP03312353	5.390×10^{-4}	5.257×10^{-4}	1.011×10^{-5}	1.031×10^{-5}	5.850×10^{-7}	1.113×10^{-3}	4.252×10^{-5}	4.00	2.9536	0.0166	104.64	
TP03271009	5.230×10^{-4}	5.257×10^{-4}	1.011×10^{-5}	1.031×10^{-5}	5.622×10^{-7}	1.069×10^{-3}	4.372×10^{-5}	4.00	2.9708	0.0178	102.92	
TP03275234 (2)	5.390×10^{-4}	5.257×10^{-4}	1.011×10^{-5}	1.031×10^{-5}	5.780×10^{-7}	1.100×10^{-3}	4.240×10^{-5}	4.00	2.9588	0.0167	104.12	
TP03324728	5.240×10^{-4}	5.257×10^{-4}	1.011×10^{-5}	1.031×10^{-5}	1.003×10^{-7}	1.908×10^{-4}	3.835×10^{-5}	5.00	3.7194	0.0873	128.06	
TP03287742	5.390×10^{-4}	5.257×10^{-4}	1.011×10^{-5}	1.031×10^{-5}	9.600×10^{-8}	1.826×10^{-4}	3.726×10^{-5}	5.00	3.7384	0.0886	126.16	
TP03348187 (2)	5.130×10^{-4}	5.257×10^{-4}	1.011×10^{-5}	1.031×10^{-5}	9.837×10^{-8}	1.871×10^{-4}	3.918×10^{-5}	5.00	3.7279	0.0909	127.21	
TP03348187	5.204×10^{-4}	5.257×10^{-4}	1.011×10^{-5}	1.031×10^{-5}	9.915×10^{-8}	1.886×10^{-4}	3.862×10^{-5}	5.00	3.7244	0.0889	127.56	

Table A.1: Measurement results for measurements of the OD values of the ND filters with the method 1. The ID is the identification number of the OD filter.

ID	$P_{\text{before}} \times 10^{-4}$ [W]	P_{after} [W]	P_{measured} [W]	T_{Measured}	$\Delta T_{\text{Measured}}$	OD _{Expected}	OD _{measured}	$\Delta \text{OD}_{\text{measured}}$	Deviation (%)
TP03337667	5.13×10^{-4}	6.98×10^{-5}	0.1361	5.32×10^{-4}	1.00	0.8660	0.0017	13.40	
TP03337667 (2)	5.13×10^{-4}	7.30×10^{-5}	0.1422	5.56×10^{-4}	1.00	0.8469	0.0017	15.31	
TP03366490	5.13×10^{-4}	4.07×10^{-6}	0.0079	3.12×10^{-5}	3.00	2.1004	0.0017	89.96	
TP03366490 (2)	5.13×10^{-4}	3.80×10^{-6}	0.0074	2.91×10^{-5}	3.00	2.1306	0.0017	86.94	
TP03275234	5.13×10^{-4}	4.86×10^{-7}	0.0009	5.37×10^{-6}	4.00	3.0235	0.0025	97.65	
TP03312353	5.13×10^{-4}	4.96×10^{-7}	0.0010	5.43×10^{-6}	4.00	3.0142	0.0024	98.58	
TP03271009	5.13×10^{-4}	4.98×10^{-7}	0.0010	5.43×10^{-6}	4.00	3.0130	0.0024	98.70	
TP03275234 (2)	5.13×10^{-4}	4.96×10^{-7}	0.0010	5.42×10^{-6}	4.00	3.0150	0.0024	98.50	
TP03324728	5.13×10^{-4}	8.75×10^{-8}	0.0002	7.71×10^{-7}	5.00	3.7682	0.0020	123.18	
TP03287742	5.13×10^{-4}	8.92×10^{-8}	0.0002	7.82×10^{-7}	5.00	3.7598	0.0020	124.02	
TP03348187 (2)	5.13×10^{-4}	9.12×10^{-8}	0.0002	7.95×10^{-7}	5.00	3.7502	0.0019	124.98	
TP03348187	5.13×10^{-4}	9.06×10^{-8}	0.0002	7.92×10^{-7}	5.00	3.7529	0.0019	124.71	

Table A.2: Measurement results for measurements of the OD values of the ND filters with the method 2. The ID is the identification number of the OD filter.

Appendix A Appendix

ID	OD _{Expected}	T_{Measured}	$\Delta T_{\text{Systematic}}$	ΔT_{Stat}	ΔT	OD _{mean}	ΔOD
TP03337667	1.00	1.43×10^{-1}	6.916×10^{-3}	3.149×10^{-3}	7.599×10^{-3}	0.8445	0.0231
TP03337667 (2)	1.00	1.47×10^{-1}	5.196×10^{-3}	2.997×10^{-3}	5.998×10^{-3}	0.8314	0.0177
TP03366490	3.00	8.27×10^{-3}	3.326×10^{-4}	1.840×10^{-4}	3.800×10^{-4}	2.0826	0.0199
TP03366490 (2)	3.00	7.93×10^{-3}	5.312×10^{-4}	1.701×10^{-4}	5.577×10^{-4}	2.1005	0.0305
TP03275234	4.00	1.00×10^{-3}	5.421×10^{-5}	4.361×10^{-5}	6.958×10^{-5}	2.9993	0.0302
TP03312353	4.00	1.04×10^{-3}	7.251×10^{-5}	4.286×10^{-5}	8.423×10^{-5}	2.9828	0.0352
TP03271009	4.00	1.02×10^{-3}	4.946×10^{-5}	4.405×10^{-5}	6.624×10^{-5}	2.9914	0.0282
TP03275234 (2)	4.00	1.03×10^{-3}	6.673×10^{-5}	4.274×10^{-5}	7.925×10^{-5}	2.9860	0.0333
TP03324728	5.00	1.81×10^{-4}	1.013×10^{-5}	3.836×10^{-5}	3.968×10^{-5}	3.7431	0.0954
TP03287742	5.00	1.78×10^{-4}	4.374×10^{-6}	3.727×10^{-5}	3.753×10^{-5}	3.7490	0.0914
TP03348187 (2)	5.00	1.82×10^{-4}	4.688×10^{-6}	3.918×10^{-5}	3.946×10^{-5}	3.7389	0.0939
TP03348187	5.00	1.83×10^{-4}	5.976×10^{-6}	3.862×10^{-5}	3.908×10^{-5}	3.7384	0.0929

Table A.3: Combined results for measurements of the OD values of the ND filters with method 1 and 2. The ID is the identification number of the OD filter.

This final values are in good agreement with the values from the manufacturer Thorlabs as shown on their website [24]. The self calculated errors even provide a narrower error range than the errors provided by Thorlabs. Unfortunately, it can not be proved how close the calculated values are to the real OD values from Thorlabs, because no exact values are given. Only a rough curve (wavelength vs OD) is provided. Here, exact determination of an expectation value can not be done.

A.3 Angle dependent count rate measurement data and results

P _{input} [W]	OD _{total}	ΔOD _{total}	P _{expected output} [W]	ΔP _{output} [W]	Δ# [MHz]	# measured
5,11E-04	9,57	0,13	1,36E-13	1,83E-14	0,072	0,437
5,11E-04	9,57	0,13	1,36E-13	1,83E-14	0,072	0,418
5,11E-04	9,57	0,13	1,36E-13	1,83E-14	0,072	0,375
5,11E-04	9,57	0,13	1,36E-13	1,83E-14	0,072	0,330
5,11E-04	9,57	0,13	1,36E-13	1,83E-14	0,072	0,310
5,11E-04	9,57	0,13	1,36E-13	1,83E-14	0,072	0,314
5,11E-04	9,57	0,13	1,36E-13	1,83E-14	0,072	0,358
5,11E-04	9,57	0,13	1,36E-13	1,83E-14	0,072	0,402
5,11E-04	9,57	0,13	1,36E-13	1,83E-14	0,072	0,438
5,11E-04	9,57	0,13	1,36E-13	1,83E-14	0,072	0,440
5,11E-04	9,57	0,13	1,36E-13	1,83E-14	0,072	0,412
5,11E-04	9,57	0,13	1,36E-13	1,83E-14	0,072	0,367
5,11E-04	9,57	0,13	1,36E-13	1,83E-14	0,072	0,323
5,11E-04	9,57	0,13	1,36E-13	1,83E-14	0,072	0,308
5,11E-04	9,57	0,13	1,36E-13	1,83E-14	0,072	0,320
5,11E-04	9,57	0,13	1,36E-13	1,83E-14	0,072	0,351
5,11E-04	9,57	0,13	1,36E-13	1,83E-14	0,072	0,399
5,11E-04	9,57	0,13	1,36E-13	1,83E-14	0,072	0,430
5,11E-04	9,57	0,13	1,36E-13	1,83E-14	0,072	0,435
5,11E-04	9,57	0,13	1,36E-13	1,83E-14	0,072	0,404
5,11E-04	9,57	0,13	1,36E-13	1,83E-14	0,072	0,353

Table A.4: Angle dependend countrate results for 5.11μW as input laser power.

A.4 Count rate dependent efficiency η_{sde}

η_{sde} [%]	$\Delta\eta_{\text{sde}}$ [%]	# _{incident} [MHz]	Δ# _{incident} [MHz]
87.242	4.955	67.363	6.797
90.408	9.529	9.575	0.991
91.834	9.550	2.446	0.139
89.760	9.448	0.531	$5.596 \cdot 10^{-2}$
90.793	9.657	0.388	$4.0314 \cdot 10^{-2}$
90.332	10.416	0.067	$7.086 \cdot 10^{-3}$
55.312	5.580	$1.230 \cdot 10^{-3}$	$1.299 \cdot 10^{-3}$
88.392	9.149	$1.802 \cdot 10^{-3}$	$0.201 \cdot 10^{-3}$

Table A.5: Efficiency values η_{sde} for different count rates. Measurement were done with 518.1μW input laser power.

A.5 Bias sweeping for different count rates

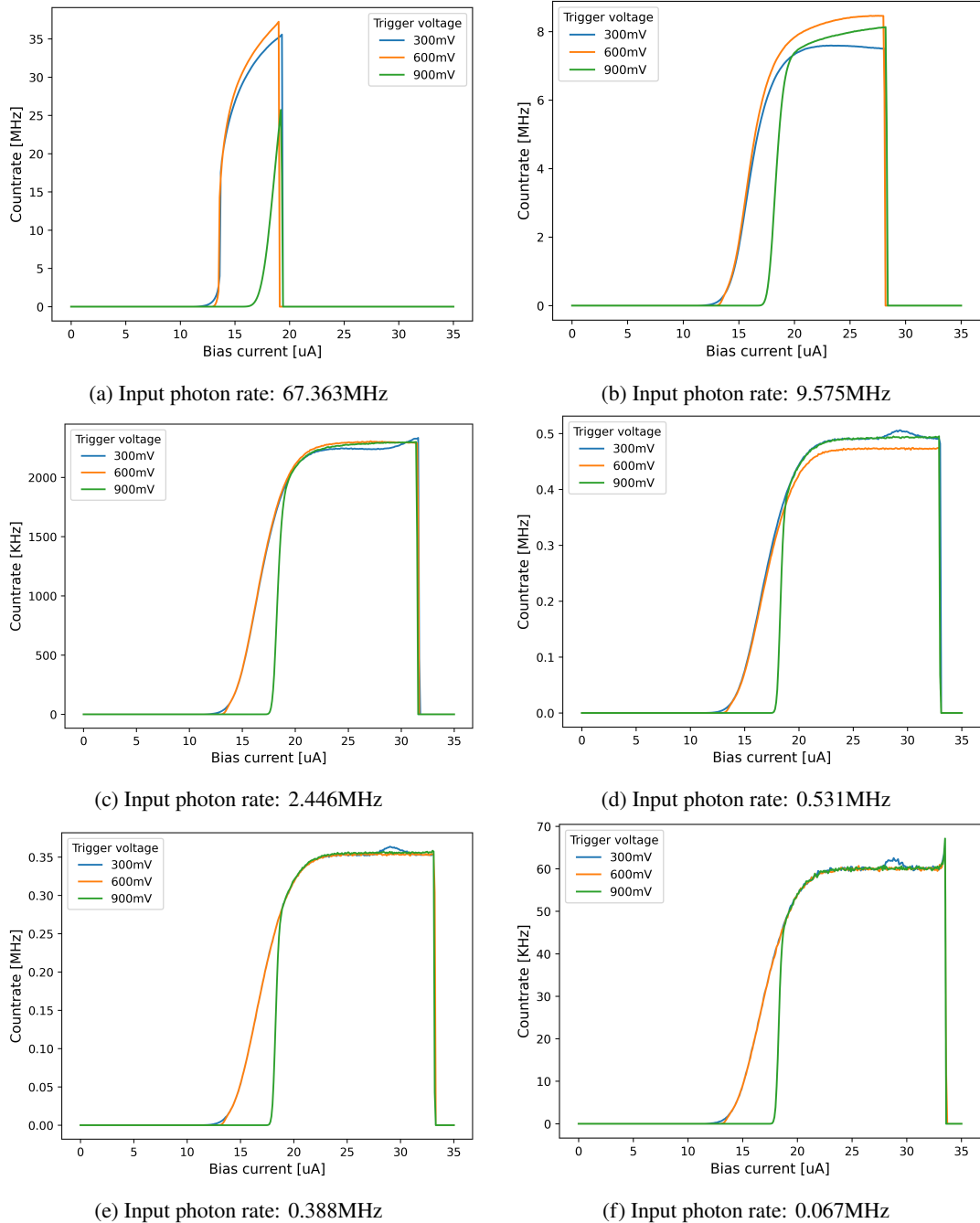


Figure A.5: Bias sweep measurement (Bias current vs. Count rate) - Error bars are not shown for better visibility.

Appendix A Appendix

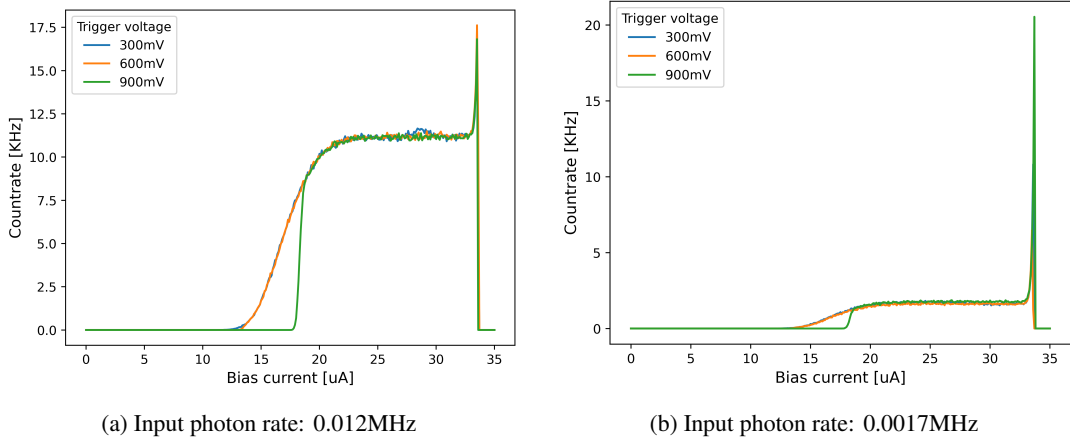


Figure A.6: Bias sweep measurement (Bias current vs. Count rate) - Error bars are not shown for better visibility.

A.6 Recovery time measurements

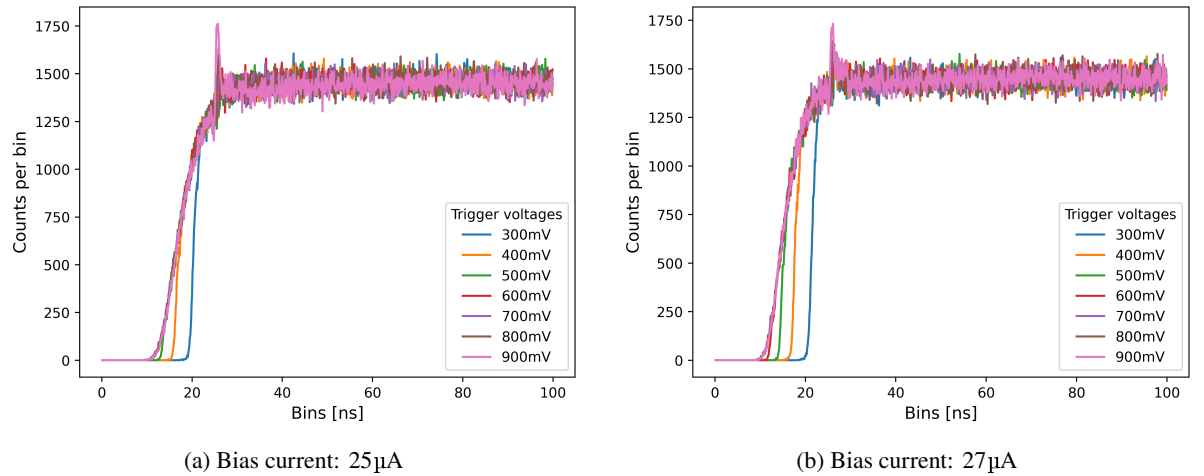


Figure A.7: Results of autocorrelation evaluation (Input photon rate: 0.531MHz) - bins are in ns and represent the different time intervals between the incoming pulses. - Error bars are not shown for better visibility.

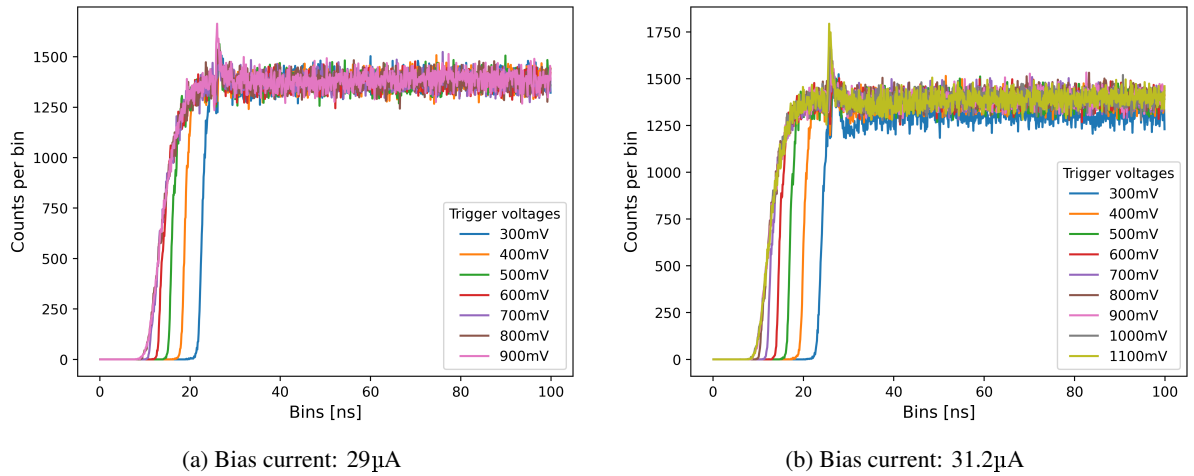


Figure A.8: Results of autocorrelation evaluation (Input photon rate: 0.531MHz) - bins are in ns and represent the different time intervals between the incoming pulses. - Error bars are not shown for better visibility.

A.7 Recordings of analog pulses

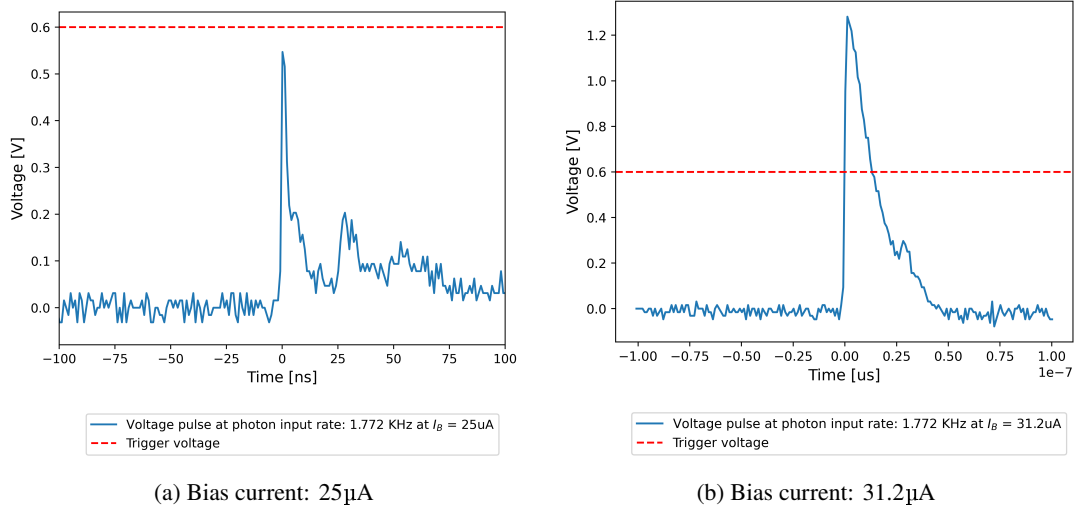


Figure A.9: Recordings of analog pulses for different bias currents. Recordings are done with oscilloscope with time resolution of 500MHz.

Appendix A Appendix

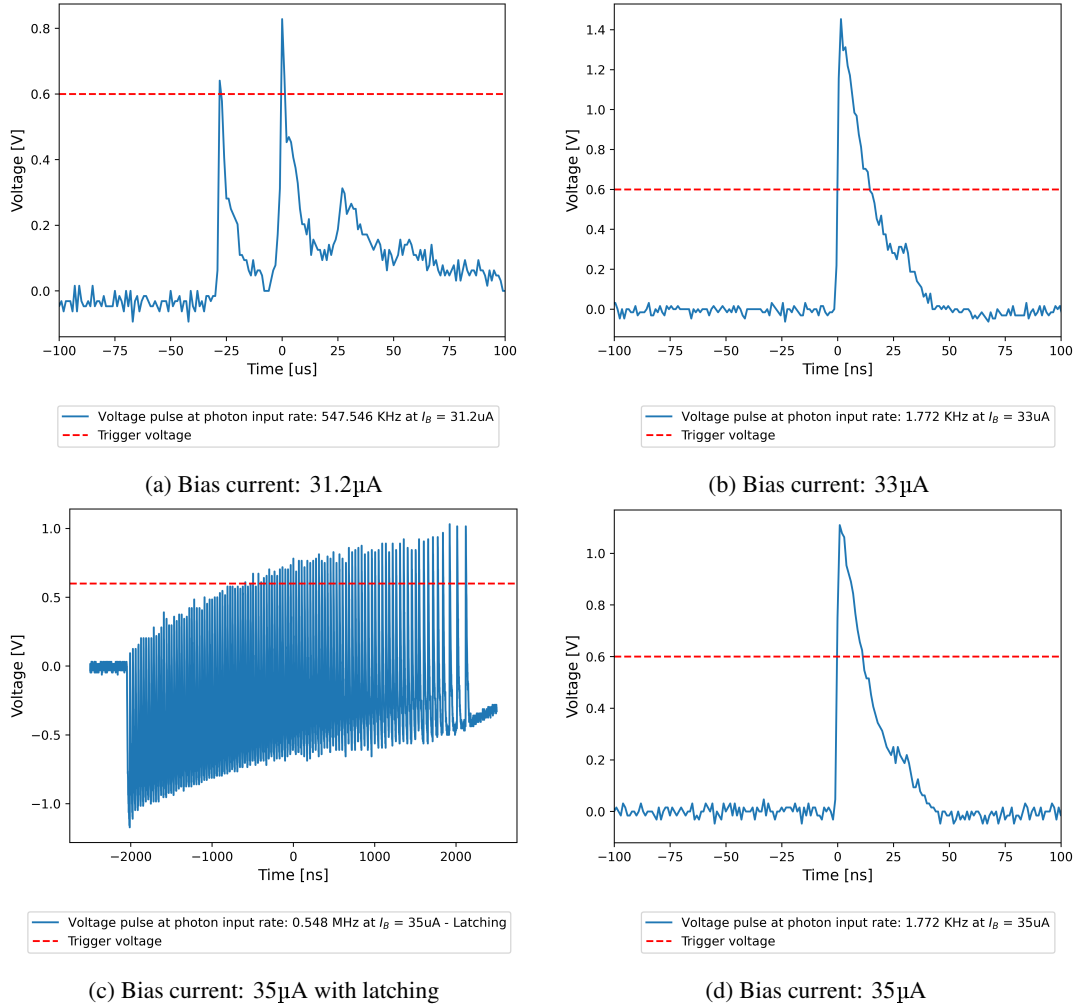


Figure A.10: Recordings of analog pulses for different bias currents. Recordings are done with oscilloscope with time resolution of 500MHz.

Bibliography

- [1] O. Firstenberg, C. S. Adams and S. Hofferberth,
Nonlinear quantum optics mediated by Rydberg interactions,
Journal of Physics B Atomic Molecular and Optical Physics **49** (2016) 152003,
URL: <https://doi.org/10.1088/0953-4075/49/15/152003>.
- [2] M. Gao, Y. Liu and X. Wang,
Coupling Rydberg atoms to superconducting qubits via nanomechanical resonator,
Physical Review A **83** (2011), URL: <https://doi.org/10.1103/physreva.83.022309>.
- [3] A. D. O'Connell et al.,
Quantum ground state and single-phonon control of a mechanical resonator, **Nature** (2010),
URL: <https://doi.org/10.1038/nature08967>.
- [4] M. D. Lukin et al.,
Dipole Blockade and Quantum Information Processing in Mesoscopic Atomic Ensembles,
Physical Review Letters **87** (2001),
URL: <https://doi.org/10.1103/physrevlett.87.037901>.
- [5] E. Urban et al., *Observation of Rydberg blockade between two atoms*,
Nature Physics **5** (2009) 110, URL: <https://doi.org/10.1038/nphys1178>.
- [6] Single Quantum, *Technical Characterization Sheet*, 2023 (cit. on pp. 11, 23–26).
- [7] G. N. Gol'tsman et al., *Picosecond superconducting single-photon optical detector*,
Applied Physics Letters **79** (2001) 705, URL: <https://doi.org/10.1063/1.1388868>
(cit. on p. 2).
- [8] C. M. Natarajan, M. G. Tanner and R. H. Hadfield,
Superconducting nanowire single-photon detectors: physics and applications,
Superconductor science and technology/Superconductor science technology **25** (2012) 063001,
URL: <https://doi.org/10.1088/0953-2048/25/6/063001> (cit. on pp. 2, 10, 17, 24).
- [9] J. Bardeen, L. N. Cooper and J. R. Schrieffer, *Theory of Superconductivity*,
Physical Review **108** (1957) 1175, URL: <https://doi.org/10.1103/physrev.108.1175>
(cit. on p. 2).
- [10] Single Quantum, *Single Quantum EOS User Manual*, 2022 (cit. on pp. 2, 3, 7, 8, 18).

Bibliography

- [11] G. A. Steudle et al.,
Measuring the quantum nature of light with a single source and a single detector,
Physical review. A, Atomic, molecular, and optical physics/Physical review, A, Atomic,
molecular, and optical physics **86** (2012),
URL: <https://doi.org/10.1103/physreva.86.053814> (cit. on p. 3).
- [12] singlequantum.com, *Superconducting Nanowire Single Photon Detectors Operation principle*,
<https://singlequantum.com/wp-content/uploads/2023/06/Single-Quantum-Operation-Principle-print.pdf>, Accessed: 2023-06, n.d. (Cit. on p. 4).
- [13] F. Zheng et al., *Design of a polarization-insensitive superconducting nanowire single photon detector with high detection efficiency*, Scientific reports **6** (2016),
URL: <https://doi.org/10.1038/srep22710> (cit. on p. 3).
- [14] Single Quantm, *Operation principle of SNSPD*,
URL: <https://www.singlequantum.com/technology/snspd/> (visited on 25/07/2024)
(cit. on p. 5).
- [15] R. H. Hadfield, *Single-photon detectors for optical quantum information applications*,
Nature photonics **3** (2009) 696, URL: <https://doi.org/10.1038/nphoton.2009.230>
(cit. on pp. 6, 7, 10, 12, 17, 25).
- [16] Wikipedia-Autoren, *Reflexionsgrad*, 2004,
URL: <https://de.wikipedia.org/wiki/Reflexionsgrad> (cit. on p. 8).
- [17] Wikipedia contributors, *Signal-to-noise ratio*, 2024,
URL: https://en.wikipedia.org/wiki/Signal-to-noise_ratio (cit. on p. 10).
- [18] K. Shalm et al., *Single-Photon Detector Tutorial*, Computer Scientist QCRYPT,
National Institute of Standards and Technology, 2013, URL: <https://qcrypt.github.io/2013.qcrypt.net/contributions/Shalm-slides.pdf>
(cit. on p. 13).
- [19] C. Autebert et al.,
Direct measurement of the recovery time of superconducting nanowire single-photon detectors,
Journal of applied physics **128** (2020), URL: <https://doi.org/10.1063/5.0007976>
(cit. on pp. 13, 26).
- [20] S. Miki, M. Yabuno, T. Yamashita and H. Terai, *Stable, high-performance operation of a fiber-coupled superconducting nanowire avalanche photon detector*,
Optics express **25** (2017) 6796, URL: <https://doi.org/10.1364/oe.25.006796>
(cit. on pp. 13, 26).
- [21] Single Quantum, *Single Quantum Eos Datasheet*, Accessed: July 27, 2024, 2019, URL: <https://singlequantum.com/wp-content/uploads/2019/05/Single-Quantum-Eos.pdf>
(cit. on p. 25).
- [22] R. J. Glauber, *The Quantum Theory of Optical Coherence*, Physical Review **130** (1963) 2529,
URL: <https://doi.org/10.1103/physrev.130.2529> (cit. on p. 27).
- [23] *Digital Handheld Optical Power and Energy Meter Console*,
URL: https://www.thorlabs.com/newgroupage9.cfm?objectgroup_id=3341
(cit. on p. 30).

Bibliography

- [24] *ND Filters: Mounted, AR Coated for 650 - 1050 nm*,
URL: https://www.thorlabs.com/newgroupage9.cfm?objectgroup_id=6274
(cit. on pp. 32, 33).